UNIVERSITY OF CALIFORNIA SAN DIEGO

Magnetic Drift Velocity Characterization of Iron Oxide- Silica Nanocarriers for Applications in Targeted Drug Delivery

A Thesis submitted in partial satisfaction of the requirements
for the degree Master of Science

in

Materials Science and Engineering

by

Vrinda Sant

Committee in charge:

Professor Ratnesh Lal, Chair
Professor Javier Garay
Professor Jeffrey Rinehart

2018

The Thesis of Vrinda Sant is approved, and it is acceptable in quality and form for publication on microfilm and electronically:

Chair

University of California San Diego

2018

TABLE OF CONTENTS

LIST OF FIGURES

ABSTRACT OF THESIS

Magnetic Drift Velocity Characterization of Iron Oxide- Silica Nanocarriers

for Applications in Targeted Drug Delivery

by

Vrinda Sant

Master of Science in Materials Science and Engineering

University of California San Diego, 2018

Professor Ratnesh Lal, Chair

Nanoparticles (NPs) are promising candidates to penetrate the blood brain barrier for delivering therapeutics to treat diseases affecting the central nervous system. However, obtaining effective doses of therapeutic NPs in disease sites is challenging due to rapid sequestering by phagocytic organs. A potential solution is to use magnetic nanoparticles (MNPs) and guide them away from undesired organs through the circulatory system. MNPs with large magnetic moments enable high guiding efficiencies in technologically feasible magnetic

field gradients ($\nabla\vec{B}$). To this end, we designed nanobowls composed of a silica core embedded with magnetic iron oxide-NPs. These nanobowls are nanoparticles featuring a bowl-like pit for drug encapsulation. Nanobowls have a large magnetic moment of $2x10^{-17}Am^2$. Guiding efficiency for nanobowls was determined *in vitro* using particle trajectories. The mathematical framework for particle trajectories involves the force balance between magnetic (F_M) and Stokes drag force (F_D). Previously, NPs with large F_M/ F_D ratio have been shown to have high guiding efficiency. Magnetic drift velocity was measured as concentration flux toward a magnet to quantify F_M. This framework can be used to predict particle trajectories. The validity was confirmed by imaging nanobowl cluster trajectories in different fluid flow and magnetic conditions. $\nabla\vec{B}$ used was larger than the average in commercial MRI machines. As expected, in 15 μm/s fluid velocity, clusters of nanobowls deviate 3° due to magnetic force. In case of physiological convection velocities often >1mm/s, framework calculations predict negligible deviation of nanobowls to the same $\nabla\vec{B}$, insufficient for high guiding efficiency. Further work is thus required to develop larger magnetic moment nanocarriers.

Chapter 1

Introduction – Motivation, Current State of Technology and Applications

Targeted Drug Delivery with Nanoparticles

Nanoparticles (NPs) with therapeutic payloads (nanocarriers) have emerged as promising candidates for targeted delivery. Targeted drug delivery aims to localize nanocarriers and increase concentration of therapeutic at a target site. This reduces systemic toxicity and side-effects to non-target tissues. Passive targeting occurs when NPs are able to penetrate through leaky vasculature found in tumors, inflamed and infected areas. Healthy tissues have tightly regulated extravasation (uptake) across the vascular endothelial membrane (blood vessel lining) that keep NPs out [1]. Active targeting entails control over drug release site and time[2]. Currently, active targeting occurs by two mechanisms: (1) *on-demand release* and (2) *site-specific localization*[3]. On-demand release is when a stimulus at the target site causes the release of encapsulated therapeutic from nanocarriers. NPs sensitive to several stimuli have been developed, including alternating magnetic field[4,5], thermal[6,7], acoustic[8] and disease environment specific (e.g. pH)[9–11]. For example, infra-red radiation induces high temperatures in magnetic nanoparticle clusters. This property has been exploited for photothermal ablation of tumors. Gold cages coated with thermally sensitive polymers have been developed for on-off drug release upon focused ultrasound stimulus[12]. The common motif with this type of targeting is that the drug release mechanism is selectively turned on by confining stimuli to the target site. Another strategy for targeting is site-specific localization. Here, NPs are modified with diseased cell-type specific ligands[13,14]. These ligands recognize and bind to diseased cells followed by NP uptake by endocytosis. Once NPs is internalized in the cell, its final fate depends on the protein involved in endocytosis[15]. In some pathways, the drug is released when NPs are digested by lysosomal enzymes. After selective attachment of NP to target cell, hyperthermia has also been

used for targeted ablation of cells. NPs with high anisotropy magnetic materials or gold enable hyperthermia-based cell death[16,17].

Nanoparticles to Treat Central Nervous (CNS) System Diseases

NPs have shown success to varying degrees in *penetrating otherwise inaccessible regions in the body*, like the brain[18]. The brain is protected by the blood brain barrier (BBB) that prevents passage of molecules larger than 400 Da, letting in only 2% of lipid soluble small molecules through the BBB by passive diffusion[19]. This selectivity poses an obstacle for drug delivery to treat central nervous system (CNS) disorders as several experimental drugs for currently uncurable diseases are kept out of diseased locations by these barriers. As populations age, CNS diseases like Alzheimer's Disease (AD) and Parkinson's Disease (PD) have become more common. Due to the impermeability of anti-cancer agents to the brain, the most common brain tumor treatment continues to be invasive intracranial surgery and aggressive radiation or chemotherapy[20].

Several methods have been developed to enhance delivery across the BBB. These include methods to increase permeability of BBB by (1) temporary disruption or (2) carrier mediated transport and (3) surpassing the BBB by using alternative delivery routes. Temporary disruption methods include drug induced osmotic pressure changes across BBB and MRI focused ultrasound. However, these methods allow the passage of unwanted substances[18,19,21]. Carrier mediated transport involves the pharmacological modification of drug molecules to resemble endogenous BBB permeable carriers[19]. Intranasal and transmucosal routes have been successful in delivering large molecules to the brain. However, not all regions of the brain are accessible via these routes[21]. Direct catheter mediated injection or pharmacological modification of drug molecules are very costly methods that are unable to keep up with rapidly increasing demand[22].

Given these limitations, nanocarriers can enable cost-effective penetration of the BBB in a controlled fashion, therefore, reducing side-effects and intake of harmful substances. The

passage of substances across the BBB is selective to properties like size, degree of lipophilicity, surface charge and ligand specificity. NPs are flexible to modification of these properties and can be tailored to fit the needs of specific tissue barriers[19,23]. Additionally, facile surface modification of NPs allows for attachment of ligands that enable receptor mediated endocytosis at the BBB. Some nanocarriers with lipophilic coatings can penetrate the BBB by passive diffusion. Using NPs as drug carriers is more effective for certain pathologies, like AD as it increase the permeability of BBB, allowing passive nanocarrier uptake[24]. Several studies have shown that modifying nanoparticles with surfactants increases uptake across the BBB[25,26]. For example, polysorbate-80 coated nanocarriers adsorb ApoE (a lipoprotein in blood plasma) and are able to undergo receptor mediated endocytosis similar to lipoproteins at BBB[27]. Additionally, NPs coated with cell surface ligands for transferrin and folate have successfully penetrated the BBB to deliver therapeutic molecules[18,19,27]. *In order to maximize the benefits achieved from controlled release and enhanced permeability, some critical limitations of nanocarriers have to be overcome.*

Limitations of Nanocarriers as Drug Delivery Agents

Nanocarriers for drug delivery are a developing technology and currently have some limitations. Two **limitations** that hold us back from harnessing their full potential are:

(1) Rapid clearance from diseased location

(2) Administration of high doses and side-effects

Rapid clearance of NPs from diseased regions happens by passive diffusion. This prevents critical drug concentrations from accumulating in order to produce an effective therapeutic impact. Currently, the solution is repeated administration of drugs or nanocarriers. However, this has its drawbacks; it not only increases the cost of treatment but also increases toxicity to healthy cells[28,29].

Mononuclear Phagocytic System (MPS) consists of phagocytic cells in several parts of the body (liver, kidney, spleen and lungs) that are tasked with internalizing and eliminating

foreign materials. 95% of nanocarriers are sequestered by the (MPS) within minutes of administration[30,31]. Adsorption of proteins from blood plasma onto nanoparticles surfaces signal phagocytic cells to internalize them and break them down with enzymes (lysosomal digestion). Nanocarriers that are internalized by the MPS do not re-enter the circulation and evoke immune-responses like inflammation and cell death. This requires administration of high doses and systemic distribution of drugs leads to side-effects due to non-specific interactions. It has been shown that surface modification of nanocarriers with molecules like poly-ethylene glycol (PEG) and biomimetic membranes reduce macrophage uptake and increase circulation time from minutes to hours[31]. However, this strategy is successful only to a small degree as 50% of administered nanocarriers continue to be sequestered by MPS despite surface modification[31].

Overcoming Limitations with Magnetic Nanoparticles

a) Magnetic Nanoparticle Drug Carriers for Increased Accumulation in Diseases Tissue

Magnetic nanoparticles (MNPs) show potential to improve accumulation in diseased tissue and reduce uptake of nanocarriers by MPS. In its current state, magnetic drug delivery is able to increase accumulation of drug loaded MNPs in a diseased location for extended periods of time. Several studies have shown that placing a magnet over diseased organs in animals can concentrate drug loaded MNPs for several hours after administration thus mitigating the need for repeated administration[28,32,33]. MNP accumulation in diseased tissue has been shown to increase by 3-25% with external magnetic fields[34–38]. Jin et.al. have shown that MNPs can cross the BBB and accumulate in high concentrations in the brain[6,37]. As magnetic fields drop off very fast with distance, this strategy works well only for superficial organs and tissues. Some progress has been made to apply this strategy to deep tissue targets for which magnetic fields should reach farther distances inside the body. For this, Hallbach arrays and control algorithms have been designed to achieve finely tuned magnetic fields reaching upto 15 cm[39–42].

b) Guiding MNPs through Blood Vessel Networks to Reduce Side-effects and Allow Administration of Smaller Doses

MNPs do not reach the target tissue in appreciable doses as their majority continues to be sequestered by the phagocytic cells in the liver and spleen. Although, external magnetic fields can increase MNP accumulation in diseased tissue, ~40% of MNPs are internalized by the liver within 30 minutes of administration and upto 80% in 1 hour[34,35,37,38]. This limitation could be alleviated if MPS (liver, spleen etc) are bypassed using magnetic fields to guide MNPs away from them. This can be achieved by controlling MNP paths through the blood stream beginning from the time of administration[43].

Guiding MNPs in the blood stream requires the application of spatially precise magnetic fields at bifurcating regions and sensitive particles with large magnetic moment. Computational and experimental studies have shown that for high guiding efficiencies in blood stream, it is necessary to confine magnetic particles to streamlines that are flowing toward the targeted direction at a bifurcation[44,45]. It has been shown that particles with large magnetic to Stokes drag force ratios can be guided into branches. This would require dynamic magnetic field gradients on the mesoscale that account for continuously changing tortuosity and unpredictable blood vessel branching. Currently, no imaging or actuation system is able to achieve such dynamic control with spatial accuracy at the mesoscale. However, for immediate applications this technology can be implemented in well studied regions of the body that have large dimensions and predictable branching geometries, provided large magnetic moment nanocarriers are available.

MNP Design Considerations for Guiding Applications

Two main properties are taken into consideration:

(1) Small size to minimize adverse effects to the BBB and immune response

(2) Large magnetic moment to maximize sensitivity to applied fields

Studies have shown that to confine MNPs in blood flow, the magnetic force acting on them has to be comparable to the drag force excreted by blood flow[44,46–50]. This requires very large magnetic moment (300 kA/m) that is yet to be physically produced in nanoparticles[51].

Magnetic moment is proportional to volume i.e. larger the volume, the greater the magnetic force acting on the particle. However, this poses a challenge for delivery across the BBB as larger particles have been shown to compromise its integrity[52]. Larger particles are also more likely to be internalized by the MPS and elicit severe immune responses[31]. Larger NPs also pose the risk of obstructing blood flow in smallest blood vessels: capillaries.

This calls for the development of innovative strategies to induce larger magnetic moments in MNPs. One approach is the use of micro-swimmers with magnetic propellers whose direction of motion is controlled by external magnetic fields[43]. However, the size scale at which this technology is currently synthesized is 1-20 um, resulting in highly sensitive magnetic response albeit compromised biocompatibility. Another approach is to encapsulate MNPs in larger cores for high magnetic moment and force. Kong et.al. and Mannell et.al. have shown that encapsulating several superparamagnetic iron oxide nanoparticles (SPIONs, ~10 nm) inside a polymeric shell can increase magnetic moment by almost 15 fold[36,53]. The challenge with increasing SPION density in a core is the demagnetizing effects of dipolar interactions that prevent maximal effects of increased volume from being achieved by reducing net magnetization[54–56].

We aim to design a magnetic nanocarrier whose paths can be controlled with an external magnetic field gradient and determine their guiding efficiency *in vitro*. Guiding efficiency is defined as the portion of administered MNPs that are able to travel in the desired direction. To this end, we synthesized iron oxide (IO)-silica nanocarriers (nanobowls) by a layer-by-layer approach wherein SPIONs are embedded on a silica template and coated with an additional layer of silica. The additional silica layer aims to minimize adverse biological sides effects of IO. These carriers contain a bowl-like cavity, for post-processing drug encapsulation. Magnetic moment on a nanobowl is increased by embedding several SPIONs on a single silica core. A 25-fold increase in magnetic force as compared to a single SPION is achieved, albeit with reduced per-particle magnetization attributed to demagnetizing dipolar interactions.

Determining Guiding Efficiency from Particle Trajectories

The therapeutic benefits of reducing systemic toxicity and increasing amount of nanocarriers reaching the target site depend on the guiding efficiency of MNPs. Ideally, 100% guiding efficiency is desired for targeted delivery. When an MNP in fluid flow is acted upon by a magnetic force, particle trajectories are an important determinant of guiding efficiency. Mathematical frameworks of fundamental equations are able to determine particle trajectories in different conditions[44,51]. This involves quantification of resultant velocity profiles from the balance of magnetic and drag force acting on a particle. Most commonly, magnetic force is derived from SQUID or VSM magnetization measurements[57]. In this work, we measure velocity due to magnetic force - magnetic drift velocity ($\vec{V}_R$), as a quantitative determinant of magnetic force. A framework of calculations and $\vec{V}_R$ measurement is suggested to determine guiding efficiency of nanobowls.

Measuring $\vec{V}_R$ is facile and enables predicting particle trajectories in physiologically relevant bifurcations. Direct measurement of $\vec{V}_R$ is then used to resolve resultant velocity from two comparable quantities – fluid velocity and magnetic drift velocity. To verify our experimental magnetic velocity measurements with the mathematical framework, nanobowl cluster trajectories were imaged in different fluid flow conditions.

In summary, to overcome limitations posed by uptake of MNPs by phagocytic organs, ***this study aims to***:

(1) Design a nanocarrier that can be magnetically guided to the brain at the aortic arch bifurcation, by-passing phagocytic organs

(2) Build an *in vitro* assay to determine guiding efficiency in physiological conditions using magnetic drift velocity to calculate particle trajectories.

Outline of this thesis:

The first two parts of **Chapter 2** discuss theoretical background for colloidal stability and nanoparticle magnetism. The third part presents the concept of magnetic drift velocity. In the last section of this chapter, fluid dynamics of MNPs in the presence of a magnetic field is discussed and the mathematical framework for determining resultant particle trajectories is presented.

Chapter 3 presents the experimental techniques used in this study. The first part focuses on layer-by-layer assembly of nanobowls. The latter parts describe experimental set-ups for determining magnetic drift velocity of nanoparticles and imaging their trajectories.

Chapter 4 is a detailed account of the experimental results. The first part presents several aspects of nanobowl synthesis and optimization considerations. The second part summarizes magnetic measurements. The third part analyzes the experimental set-up for determining magnetic drift velocity and its significance. The last part focuses on confirming conclusions made from theoretical work and experimental results by imaging nanobowl cluster trajectories in different conditions.

Chapter 5 presents a summary of the current work and future steps.

Chapter 2

Theoretical Considerations

2.1 Colloidal Stability

Colloidal stability is the ability of particles to remain dispersed in suspension over long periods of time against the forces of sedimentation and flocculation. Inter-particle interactions can make it favorable for particles to cluster together and form aggregates. Flocculation is undesirable because it compromises the kinetic independence of particles causing inhomogeneity in magnetic and fluidic properties. Cluster formation may be induced due to attractive forces between particles, for example, van der Waals (VDW) forces and chemical crosslinking. In magnetic colloids, an additional force from magnetic dipoles can also cause aggregation. According to the DLVO theory, the stability of a colloid is dependent on the net interaction of attractive VDW forces and repulsive electrostatic forces. Strategies to increase colloidal stability include modulating electrical double layer thickness and steric stabilization with polymers[58].

2.1.1 Sedimentation

The energy barrier for gravitational sedimentation (E_g) has to be greater than the thermal energy (E_T) for particles to remain suspended in solution[59].

$$E_T = k_B T = 3.9\ x\ 10^{-21}\ J \quad (2.1)$$

$$E_g = \Delta\rho g V h \quad (2.2)$$

Where:

k_B= Boltzmann constant = $1.3\ x\ 10^{-23} JK^{-1}$; T = Temperatures; $\Delta\rho$ is the difference of density of particles and suspension solvent; g = 9.8 m/s^2; V = volume of particle; h = height of settling. For a silica particle of radius 140nm, density 2600 kg/m^3 in water and a settling height of 2cm, $E_g = 3.6\ x\ 10^{-18} J$. Particles in this solution will not sediment as the gravitational energy barrier is three orders of magnitude greater than thermal energy.

The density of a particle made of more than one material is given by[60]:

$$\rho_{NP} = \frac{\rho_{n1}V_{n1}+\rho_{n2}V_{n2}+\cdots+\rho_{ni}V_{ni}}{V_{particle}} \text{ where } n_i \text{ is material 1,2,3…}i \quad (2.3)$$

2.1.2 van der Waal's Attraction

Particles may have permanent dipoles due to the presence of polar molecules on their surface. Permanent dipoles may initiate charge separation in a non-polar molecule identified as an induced dipole. Interactions between dipoles are a result of an electric field produced by one dipole acting on another. At separation greater than the length of the dipole, an electric field from one dipole induces a proportional and opposite dipole moment in the second molecule[58]. Three types of van der Waal's attraction can be present:

1) Permanent dipole – permanent dipole interaction

2) Permanent dipole – induced dipole interaction

3) induced dipole – induced dipole interaction (London dispersion)

In non-polar molecules, constantly deforming electron clouds interact and induce instantaneous dipoles in adjacent molecules. This is the basis for London dispersion forces and occurs in all molecules. These forces can be scaled up for nanometer- micrometer dimensions by integrating interactions over the macroscope surfaces. For two spheres of equal radii (*R*), the potential energy over separation (*s)* is[58]:

$$V_{VDW} = -\frac{AR}{12s} \quad (2.4)$$

Where A is the Hamaker constant and depends on the colloid material and solvent; for silica in water it is $8.3\ x\ 10^{-21} J$ [61]. The negative sign indicates that these forces are attractive.

2.1.3 Electric Double layer and Electrostatic repulsion

Adsorption of ions from the solvent at the solid-liquid interface gives rise to an electric potential that extends at distance, *x* from the surface. Stern layer is the region of oppositely charged ions (from that of the particle surface) that adsorb onto the surface. A diffuse layer of loosely attracted ions similar to particle surface forms around the stern layer.

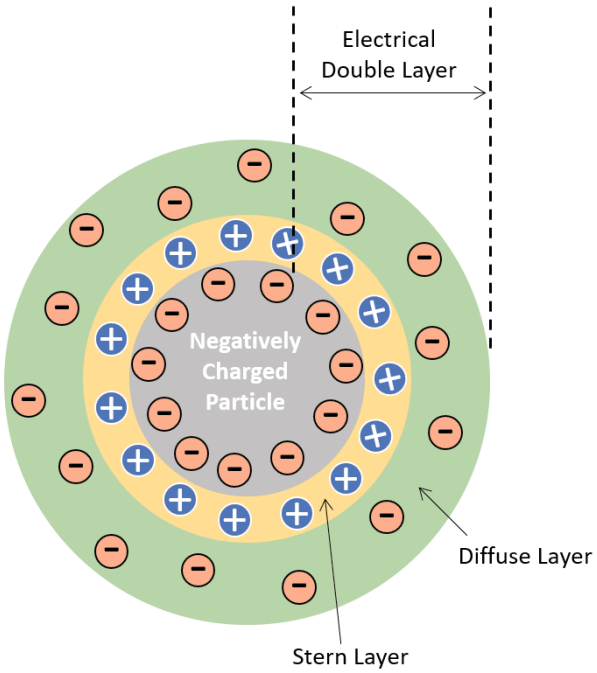

Figure 2.1: Electrical Double Layer around a negatively charged nanoparticle

Together, these layers are referred to as the electrical double layers and the inverse of their extent is called the Debye length[58] κ^{-1}. Debye length is dependent on the ionic concentration and valence of electrolytes in the solvent. The electrical potential (φ) decays exponentially from that on the solid surface (φ_0) with the relationship[58]:

$$\varphi = \varphi_0 \exp(-\kappa x) \quad (2.5)$$

Equation (2.5) shows an exponential dependence on Debye length, indicating that ionic strength plays an important role in colloidal stability: higher ionic strengths lead to more compact and dense stern layers. It follows, that the electrical potential will drop off faster for higher molarity solvents. For two spherical particles, the potential energy barrier due to electrical repulsion is[62,63]:

$$V_{repulsion} = 2\pi\varepsilon R{\varphi_0}^2 \exp(-\kappa s) \quad (2.6)$$

Where: ε= permittivity of a substance ($7\ x10^{-10} F/m$), and s is the separation. φ_0 can be estimated by the zeta potential (ζ), the electrical potential at the boundary of the Stern layer and

diffuse layer. This can be measured experimentally by electrophoretic measurements and gives a lower bound for surface potential.

2.1.3 Derjaguin – Landau - Verwey – Overbeek (DLVO) Theory

DLVO theory suggests that the net interaction potential (V_{net}) between two colloidal particles is the sum of the VDW attraction forces and electrostatic repulsive forces. The equation then for two spherical particles separated by distance *s* is:

$$V_{net} = V_{repulsion} + V_{VDW} = 2\pi\varepsilon R{\varphi_0}^2 \exp(-\kappa s) - \frac{AR}{12s} \qquad (2.7)$$

Figure 2.2 shows the variation of net interaction potential as a function of zeta potential. It can be seen that at small zeta potentials interaction energy is negative and will lead to instant flocculation. At large zeta potentials interaction energy is always positive indicating that repulsive forces dominate and the colloid is stable. At intermediate zeta potentials, the colloidal suspension is stable for a limited period of time due to the presence of a secondary minimum in the interaction energy curve. If the secondary minimum energy is small enough, the colloid can be resuspended into suspension with agitation and the flocculation is reversible.

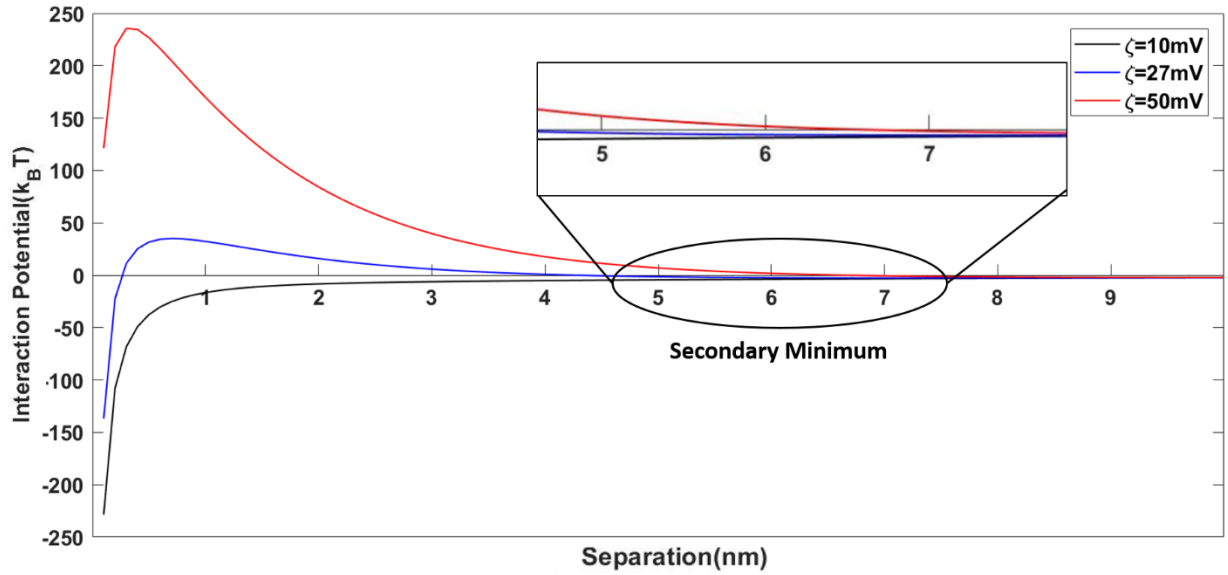

Figure 2.2: Variation of net interaction potential from Equation (2.6). A = 8.3 x $10^{-21}J$, R = 137nm, $\varepsilon = 7\ x10^{-10}F/m$, $\kappa = 0.7nm$.

If the rate of two particle cluster formation is the same as the rate at which two particles collide, the rate equation for N particles/m^3 can be written as:

$$-\frac{dN}{dt} = kN^2 \quad (2.8)$$

Where *k* is the aggregation rate constant. Integrating equation (2.8) gives:

$$\frac{1}{N} - \frac{1}{N_0} = kt \quad (2.9)$$

Where N_0 is the initial concentration of dispersed particles. Smoluchowski used Fick's first law to find the rate constant if there was no energy barrier for flocculation (k_r)[58,61]. If an additional term to account for resistance to flocculation is added to Fick's first law, the slow flocculation rate constant (k_s) can be estimated by the height of the secondary minimum.

$$k_r = \frac{k_B T}{3\eta} \quad (2.10)$$

$$k_s = k_r \exp\left(\frac{-Vsecondary}{k_B T}\right) \quad (2.11)$$

Where η = solvent viscosity and $V_{secondary\ is}$ the height of the secondary minimum. The aggregation constant and time for 50% aggregation for secondary minimum heights in Figure 2.2 is illustrated in Figure 2.3.

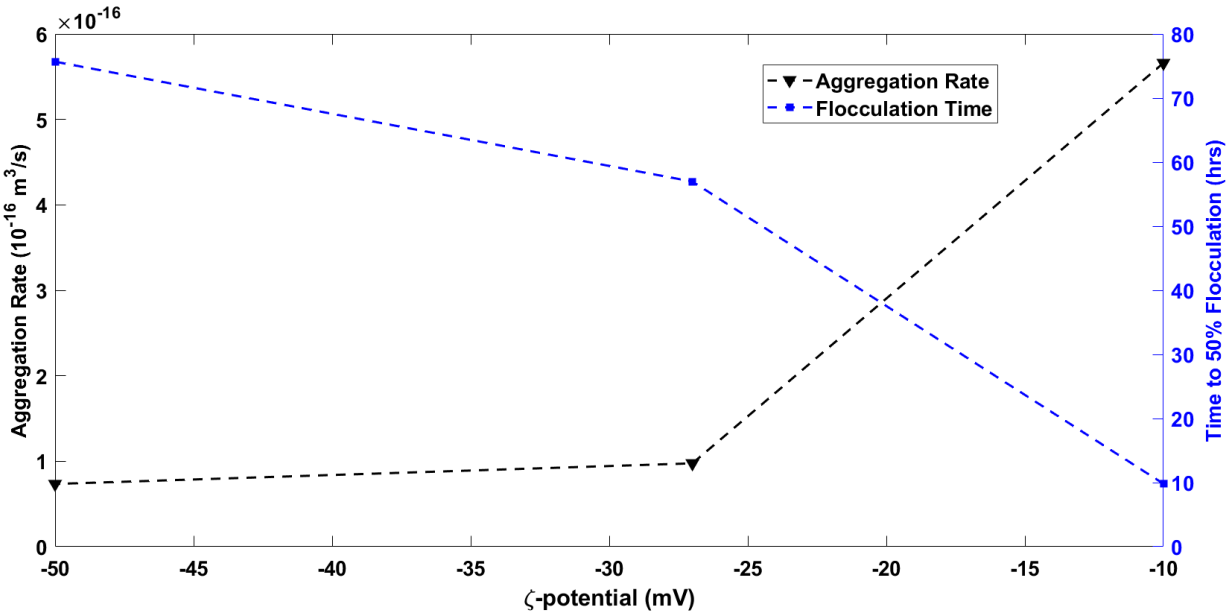

Figure 2.3: Aggregation Rate constant and time to 50% flocculation of 137nm silica particles in water. N_0=5x10^{10} particles/m^3

2.1.4 Steric Stabilization

At high ionic strengths, electrostatic potentials drop off faster, resulting in flocculation. In such situations, polymers maybe adsorbed onto particle surfaces to stabilize their suspensions. Steric stabilization is conferred as polymer shells of colliding particles overlap and only certain overlapping configurations are entropically possible. The interaction potential of two overlapping polymer shells is dependent on number of adsorbed polymer sites and its radius of gyration[64]:

$$V_{steric} = N_s k_B T \theta \pi \, (\delta - x)^2 \left(\frac{D + \delta + x}{\delta}\right) \qquad (2.12)$$

Where N_s is number of adsorbed polymer units per unit area, θ is the surface coverage, δ is the radius of gyration and $x = R\text{-}s$ (R = radius, s = separation). Equation 2.12 is only valid for separations less than the radius of gyration. Figure 2.4 shows a comparison between the $V_{repulsion} + V_{VDW}$ from equation (2.7) V_{steric} from equation 2.12 and $V_{net\ interaction} = V_{repulsion} + V_{VDW} + V_{steric}$.

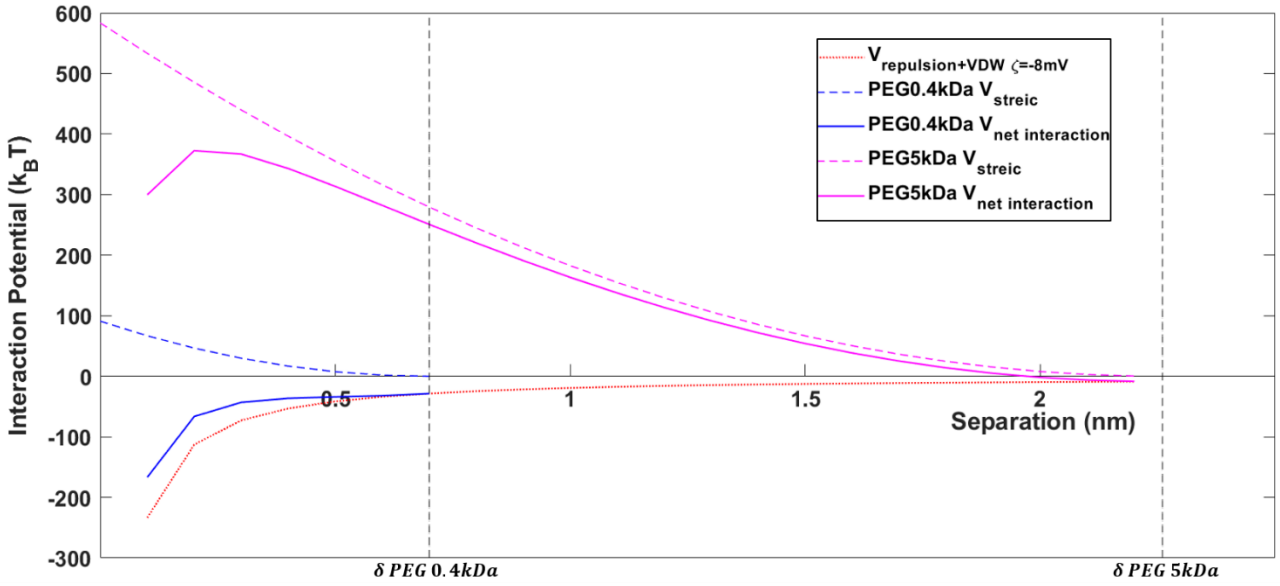

Figure 2.4: Interaction energies from Equation (2.6) and (2.11) and $V_{net\ interaction}$ from sum of both equations. $\zeta = -8\,mV$, θ=0.2. PEG 0.4kDa: N_s=1.5 x10^{18} m^{-2}, δ = 0.7nm. PEG 5kDa: N_s=2.95 x10^{18} m^{-2}, δ = 2.26nm[65].

2.1.5 Magnetic Dipole Interactions

Magnetic particles may have enough moment in some external fields to attract each other in solution. In this case, the lowest energy configuration would be to cluster together in the direction of the field. Such aggregation may be reversible depending on the anisotropy of the cluster. The equation for interaction potential of magnetic dipoles is given as[66]:

$$V_{dipole} = \frac{\mu_0}{4\pi}\left[\frac{m_1 m_2 - 3\,(m_1.e_1)(m_2.e_2)}{|s^3|}\right] \qquad (2.13)$$

If both particles have equal moment and are in the same direction as the applied field, equation (2.13) can be simplified to:

$$V_{dipole} = \frac{-\mu_0 |m|^2}{4\pi |s^3|} \qquad (2.14)$$

Where: μ_0 is the permeability = $4\pi\ x\ 10^{-7} NA^{-2}$, m = moment (Am^2), s = separation, e = unit vector of dipole. Figure 2.5 shows the dipole interaction energy as a function of magnetic moment – as the moment increases, the attractive force increases. Figure 2.6 shows the net

interaction energy in the presence of VDW attraction, electrostatic repulsion and dipole attraction. For small moments the net interaction is repulsive, maintaining colloidal stability.

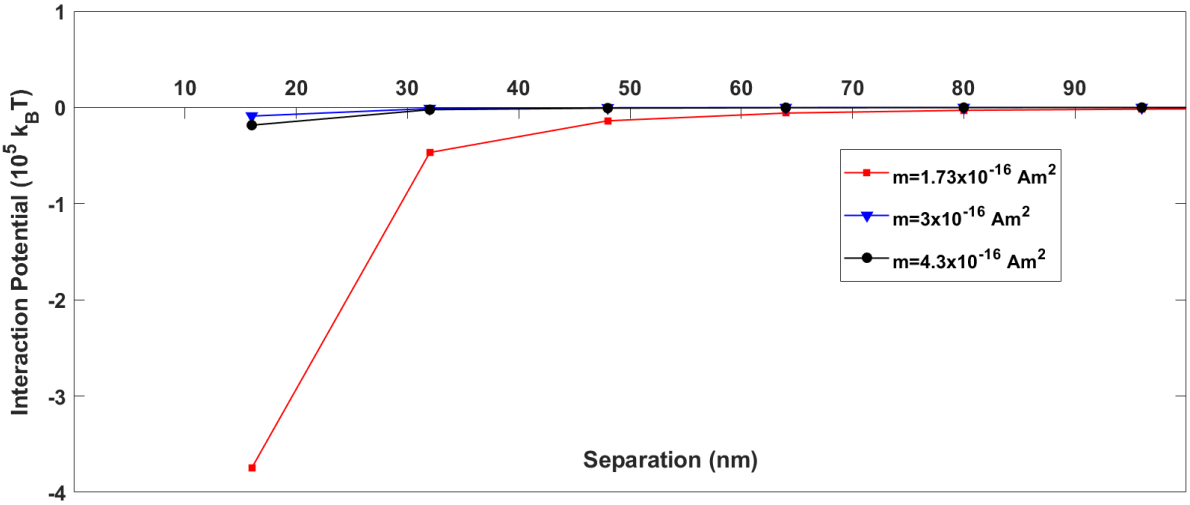

Figure 2.5: Dipole interaction energy as a function of magnetic moment.

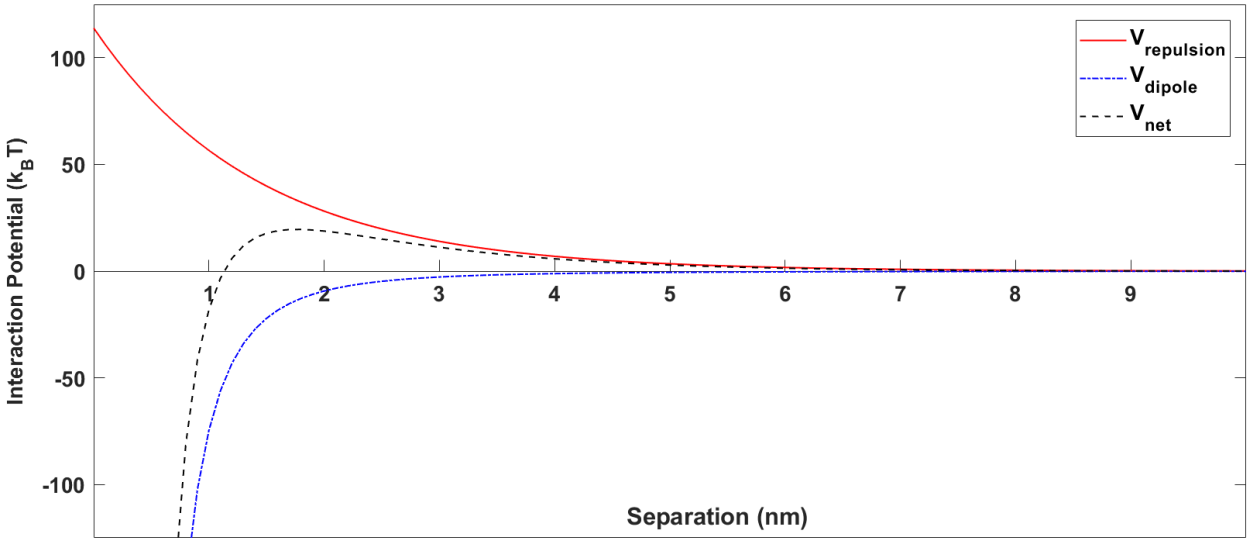

Figure 2.6: Net interaction energy (sum of equations (2.7) and (2.14)) for 137nm silica particles, $\zeta = -27\ mV$, $m = 1.73\ x\ 10^{-16} Am^2$.

2.2 Magnetic Nano-particles

2.2.1 Classification of Magnetic Materials

The bulk behavior of magnetic nanoparticles (MNPs) can be classified into diamagnetic, paramagnetic, ferromagnetic, ferrimagnetic and antiferromagnetic (Figure 2.7a). In diamagnetic

materials magnetic dipoles align themselves opposite to the applied field; no dipoles are present in the absence of a field. Therefore, the slope on Magnetization vs Field (MvsH) plot (Figure 2.7b) is negative for such materials. Paramagnetic materials have assembled dipoles which align themselves with a magnetic field. The number of aligned dipoles increases as the field increases, giving it a positive slope on the MvsH plot. Ferromagnetic and ferrimagnetic materials have net magnetism at zero external fields (M_r *remanence magnetization*) as majority of their dipoles are aligned in one direction. In ferrimagnetic and antiferromagnetic materials, dipoles arrange themselves in an antiparallel fashion, reducing or completely cancelling the any dipolar effects. At high enough external fields, all dipoles in certain materials will be aligned with the field to give the highest possible magnetization (M_s s*aturation magnetization*). The external field required to give zero magnetization is called coercivity (H_c).

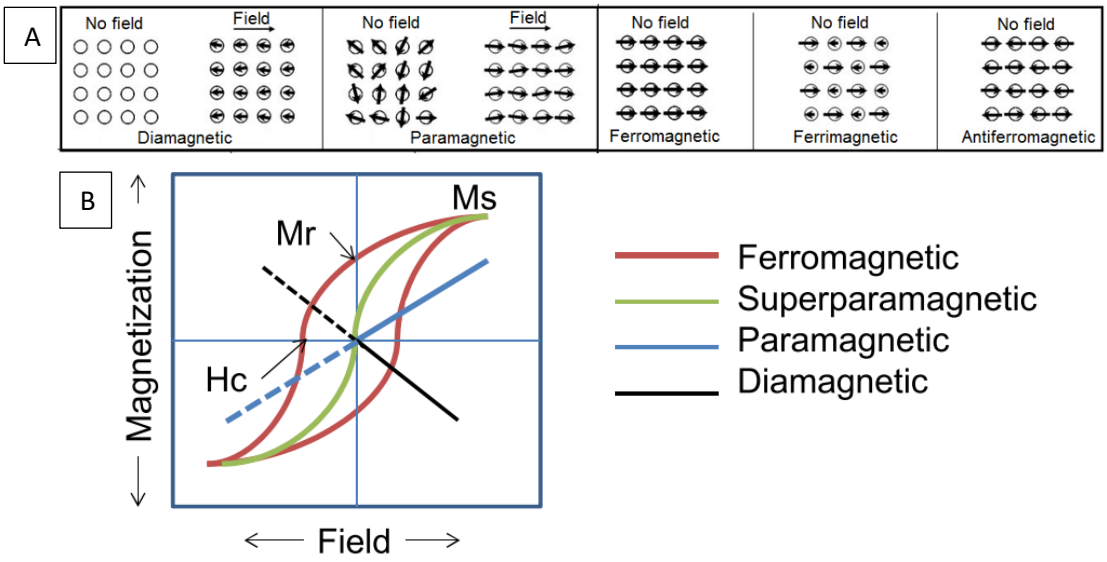

Figure 2.7:(a) Magnetic dipole arrangement (Reproduced with permission from [67]) (b) Hysteresis curves for different classes of magnetic materials (Reproduced with permission from [68]).

2.2.2 Stoner- Wohlfarth Model for MNPs

A ferromagnetic nanoparticle has an easy axis along which it is spontaneously magnetized due to an energy barrier that separates the possible orientation states that it can achieve. This anisotropy could arise due to stress in the crystal (magneto-crystalline) or shape

of the particle. A Stoner-Wohlfarth particle has an ellipsoidal shape with an easy axis along its longest dimension (Figure 2.8a). Its anisotropy energy (Figure 2.8b(ii)) is given by[59,69]:

$$E_a = K_u V sin^2(\varphi - \theta) \quad (2.15)$$

Where K_u is the anisotropy constant and V is the particle volume.

In the presence of no field, the anisotropy energy barrier prevents nanoparticles moments from changing orientations. The application of an external field in the downward direction increases the energy of the opposite orientation, lowering the energy barrier and making moment flipping possible (Figure 2.8b). The energy upon the application of an external field (H) is given by the Zeeman energy[59,69]:

$$E_z = -\mu_0 M_s H V cos(\varphi) \quad (2.16)$$

$$E_n = K_u V sin^2(\varphi - \theta) - \mu_0 M_s H V cos(\varphi) \quad (2.17)$$

The net energy (E_n) is then given by equation (2.17). Applying a field in the easy axis direction ($\theta = 0°$), results in a perfectly square hysteresis. Here, coercivity (H_c) is equal to the anisotropy field (H_a) and can be used to estimate the anisotropy constant:

$$H_c = H_a = \frac{2K_u}{\mu_0 M_s} \; for \; \theta < 45°$$

$$H_c < H_a \; for \; \theta > 45° \quad (2.18)$$

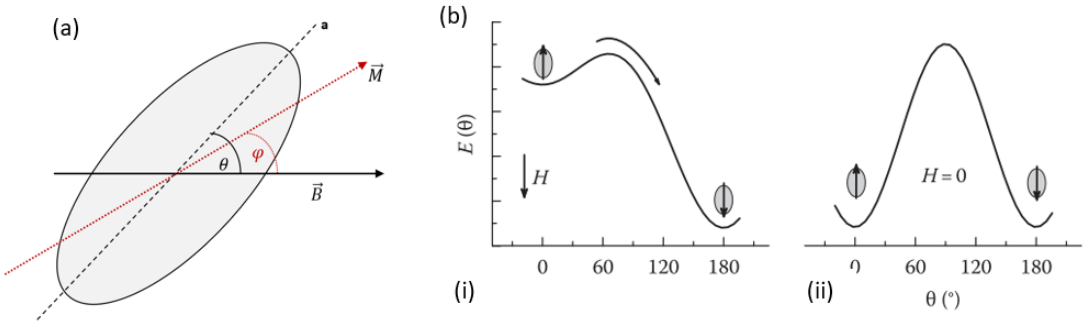

Figure 2.8: (a) Stoner-Wohlfarth particle (b) Anisotropy energy barriers (reproduced with permission from CRC Press[59])

2.2.3 Relaxation Times

A nanoparticle can align itself with an external magnetic field in two ways- (1) by changing the orientation of all its spins or (2) by physically rotating in the direction of the field. The process by which a magnetic field provides enough energy for spins to overcome the anisotropy energy barrier and change orientation is called *Nèel relaxation.* The characteristic time associated with this is given by the equation:

$$t_n = t_0 \exp(\frac{K_u V}{k_B T}) \quad (2.19)$$

Where $t_0$is a time constant dependent on the materials and ranges from[59,70] 10^{-9} -10^{-13}s, K_uV represents the anisotropic energy barrier and T is temperature. The relaxation process by which a particle rotates itself to align with the field is called *Brownian relaxation* and is given by:

$$t_B = \frac{3V_h \eta}{k_B T} \quad (2.20)$$

Where V_h is the hydrodynamic volume and η is the viscosity of the solvent. For any diameter, the fastest process defines how the particle will align itself to a field- Figure 2.9 shows that for magnetite particles smaller than 12nm, Nèel relaxation dominates and for larger ones, particle rotation faster than spin re-orientation. K_u, the anisotropy constant can be estimated from

$$K_u = \frac{H_a \mu_o M_s}{2} \quad (2.21)$$

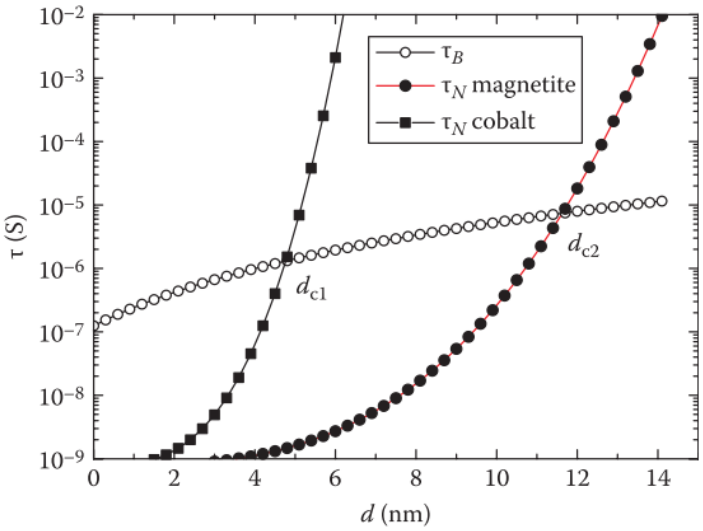

Figure 2.9: Nèel relaxation and Brownian relaxation times as they change with nanoparticle diameter for K_u magnetite = ~1.7x10^4 Jm^{-3} and cobalt = 4.3x10^5 Jm^{-3} according to equations (2.19) and (2.20)[59]*.*

2.2.4 Superparamagnetism

Below a critical radius and above a certain temperature, ferro- and ferri- magnetic materials are superparamagnetic (SPM) i.e. thermal energy is greater than the anisotropic energy barrier for moment reversal resulting in rapid random flipping of moments[59,70]. Such materials don't show remanence magnetization or coercivity and respond with high sensitivity to external magnetic fields, reaching saturation much faster than ferromagnetic materials. A certain amount of thermal energy is required to overcome the anisotropic energy barrier to induce random flipping. This happens at temperatures higher than the *blocking temperature* (T_B) where time average magnetic moment is zero[70]. Experimentally, blocking temperatures are dependent on how fast the moment is being measured. The time required for nanoparticle's moment to complete an oscillation is called the relaxation time. If the time frame of the measurement is greater than the relaxation time, zero average moment will be read and particles will be superparamagnetic. Alternatively, if the measuring time is shorter than relaxation time, the nanoparticle moment is considered to be blocked. T_B can be identified from the peak of a

magnetization vs temperature plot. Blocking temperatures can be estimated if the anisotropy constant (K_u) is known from the equation:

$$t_m = t_0 \exp(\frac{K_u V}{k_B T_B}) \quad (2.22)$$

Where t_m is the measuring time (DC measurements 60-100s[59]), $t_0$is a time constant dependent on the materials and ranges from[59,70] 10^{-9} -10^{-13}s, V is magnetic volume of the nanoparticle and T_B is the blocking temperatures. For these values, the equation can be simplified to:

$$T_B = \frac{K_u V}{25 k_B} \quad (2.23)$$

M vs H plots for superparamagnetic nanoparticles can be modeled as a group of paramagnetic ions with one large moment with the Langevin equation:

$$M = nm \left[coth\left(\frac{\mu_0 mH}{k_B T}\right) - \frac{k_B T}{\mu_0 mH} \right] \quad (2.24)$$

Where n = number of SPM particles, m= magnetic moment, H is the applied field. Equation 2.16 is not valid for particles with high anisotropy and interparticle interactions[59]. $M_s = nm$.

In bulk ferromagnets, internal energy is minimized by the formation of magnetic domains, regions where all moments are aligned in the same direction without an external field. When the size is reduced, there are critical dimensions at which, the formation of domains does not lend any energy stabilization to the sample and the particle exists as a single-domain with one 'superspin'[59]. Upon further reduction in size, thermal energy takes precedence and random moment flipping is induced, demarking the dimensions for a material to be in the SPM regime. This critical radius can be estimated from equation (2.23):

$$r_{SPM} = \sqrt[3]{\frac{6 k_B T}{Ku}} \quad (2.25)$$

The SPM radius for magnetite is 12.2nm given an anisotropy constant of 1.35x104Jm-3 for bulk magnetite[59]. Above 12.2nm, magnetite will exist as a single-domain particle with

remanence magnetization and coercivity up to a critical dimension, after which it will have multiple domains.

2.3 Magnetic Nano-particles in Fluid

2.3.1 Magnetic Force

(Bold letters indicate vector quantities)

In the presence of an external magnetic field (**H**= **B**/μ_0; **B** = magnetic flux density), a magnetic dipole moment (**m**) is induced in the magnetic nanoparticles (NPs). In the absence of inter-particle interactions and after moment relaxation in the direction of applied field, moment can be expressed as[48,49,69]. The second part of the equality is only valid for the linear portion of the hysteresis curve:

$$\boldsymbol{m} = V_m M_s = V_m \chi \boldsymbol{H} \tag{2.26}$$

Where V_m is the magnetic volume, χ is the difference in magnetic susceptibility between particles and surrounding fluid and **H** is the applied field. Superparamagnetic susceptibilities are usually one- two orders of magnitude greater than diamagnetic susceptibilities[71]. The force acting on a magnetic particle under an external magnetic field is then:

$$\boldsymbol{F_m} = (\boldsymbol{m} \cdot \nabla)\boldsymbol{B} \tag{2.27}$$

If it is assumed that a magnetic field is only acting in the y- axis and induces a magnetic moment in the same direction equation (2.26) is:

$$\boldsymbol{F_{m,y}} = \boldsymbol{m}\frac{dB}{dy} = V_m \chi \boldsymbol{H}\frac{dB}{dy} = \frac{4\pi r_m^3}{3}\chi \boldsymbol{H}\frac{dH}{dy}\mu_0 \tag{2.28}$$

Where, r_m is the volume equivalent radius of the magnetic portion of the nanoparticle. From equation (2.26) we can see that magnetic force shows cubic dependence on magnetic radius $\boldsymbol{F_m} \alpha\, r_m^3$. Therefore, the magnetic force acting on clusters of particles is stronger than that on single particles in the absence of inter-particle interactions.

2.3.2 Magnetic Drift Velocity

In a suspension of MNPs, the application of a magnetic force leads to the acceleration of the particle in direction of the force until an equilibrium velocity ($\boldsymbol{V_R}$) is reached. This equilibrium velocity is identified as *magnetic drift velocity*. An equal and opposite Stokes drag force ($\boldsymbol{F_D}$) acts on the particles (Figure 2.11b):

$$\boldsymbol{F_D} = 6\pi a\eta \boldsymbol{V_R} \tag{2.29}$$

Where *a* is the hydrodynamic radius of the particle and η is the fluid viscosity. The equilibrium velocity on the particle can then be found from a force balance[49,72]:

$$\boldsymbol{F_m} + \boldsymbol{F_D} = 0$$

$$\boldsymbol{V_R} = \frac{\boldsymbol{F_m}}{6\pi a\eta} \tag{2.30}$$

It can be seen from equation (2.28) that drag force has a linear relationship with particle radius, thus having a smaller effect on equilibrium velocity than magnetic force. Figure 2.10(a) shows the comparison between the trend of $\mathbf{F_m}$ and $\mathbf{F_D}$ with particle radius for a V_R of 1um/s, H=1000Oe and $\partial H/\partial x$ = 0.17T/cm. Figure 2.10(b) shows the that equilibrium velocity increases quadratically if a = r_m.

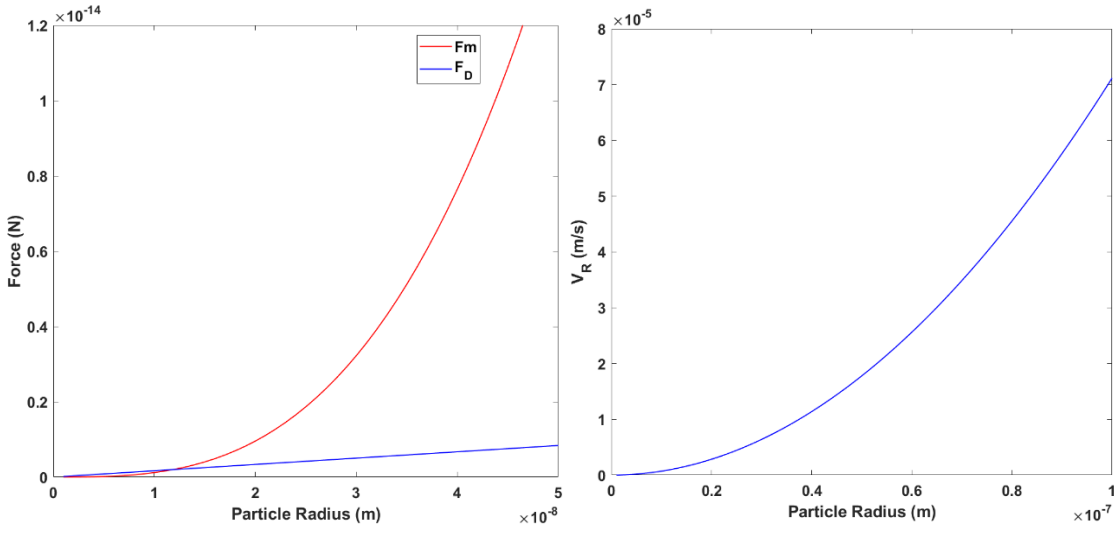

Figure 2.10: (a) Magnetic force and Stokes drag (b) Magnetic drift velocity as a function of particle radius.

2.4 Mathematical Framework for MNP trajectory in Advection

In the absence of any external forces, particle motion is a result of thermal collisions and is described as Brownian motion (Figure 2.11a). This random particle motion is a result of thermal vibrations in the particle and solvent molecules. Every time the particle moves in a certain direction, an opposing frictional drag force acts on it. The ratio of thermal energy and frictional energy is given by the Stokes diffusion coefficient:

$$D = \frac{k_B T}{6\pi\eta a} \tag{2.31}$$

In the presence of advection (fluid flow) in a microchannel, assuming no-slip between particle and fluid flow, the Stokes drag in convection ($\boldsymbol{F_{D,c}}$) can be written as[72]:

$$\boldsymbol{F_{D,c}} = 6\pi a\eta(\boldsymbol{V_l} - \boldsymbol{V_p}) \tag{2.32}$$

Where: $\boldsymbol{V_l}$ is the fluid flow velocity, and $\boldsymbol{V_p}$ is the particle velocity. In the absence of a magnetic field $\boldsymbol{V_p} = \boldsymbol{V_l}$, indicating that the particle will flow in the direction of the fluid in agreement with the no slip assumption (Figure 2.11c).

Upon the application of an external magnetic field, the particle will accelerate in the direction of magnetic force and equilibrate with magnetic force. At equilibrium $\boldsymbol{F_{D,c}} + \boldsymbol{F_m} = \boldsymbol{0}$. Then, net particle velocity can be written in terms of two force vectors[47,72,73] and can be used to determine particle trajectories in different conditions:

$$\boldsymbol{V_p} = \frac{\boldsymbol{F_m}}{6\pi a\eta} + \boldsymbol{V_l}$$

Substituting equation (2.29) and assuming that magnetic drift velocity is perpendicular to fluid flow (Figure 2.11d):

$$\boldsymbol{V_p} = \boldsymbol{V_R} + \boldsymbol{V_l} = V_R\begin{pmatrix}\boldsymbol{0}\\ \boldsymbol{1}\end{pmatrix} + V_l\begin{pmatrix}\boldsymbol{1}\\ \boldsymbol{0}\end{pmatrix} \tag{2.33}$$

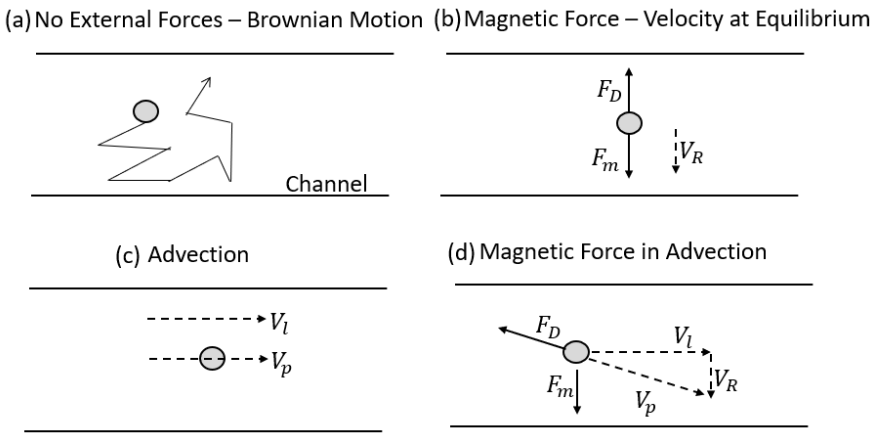

Figure2.11: MNP behavior under various forces

Chapter 3

Experimental Details

3.1 Particle Synthesis

3.1.1 Janus Template

Polystyrene- silica Janus templates were synthesized with a modified Stöber's process as described in [74,75]. In short, a silica precursor and carboxylate modified polystyrene sphere added to a polymerization buffer of water, alcohol and ammonium hydroxide. In a glass vial 700uL DI water, 4mL Isopropanol (IPA; Acros Organics) and 1.3mL Ammonium hydroxide (NH_4OH; 28%; Sigma Aldrich) were added in order and stirred for a few minutes. To this, 55uL Tetraethyl orthosilicate (TEOS; Sigma Aldrich) and 100uL polystyrene spheres (Carboxylate modified; 100nm, 2.7% in water; Ocean Nanotech) were added together. The reaction as stirred for two hours at room temperature and spun at 500g for 5 minutes to remove large chunks. The supernatant was then washed in 200 proof Ethanol (EtOH; Koptec) three times at 3221g for 10 minutes each time. After the final wash, the pellet was resuspended in 4mL EtOH and sonicated for 10 minutes.

3.1.2 Amine Modification

The silane surface was silanized with an amino-silane for Iron Oxide attachment. 4.32uL (3-Aminopropyl) triethoxysilane 99% (Sigma Aldrich) was added to the above mixture and it was stirred in 60°C for 2 hours. The reaction mixture was washed three times in EtOH at 3221g for 10 minutes each time. Particles were resuspended in EtOH and cured in a vacuum oven overnight at 60-80°C for covalent silane binding[76]. Particles should not be exposed to water until after the curing step to avoid disturbing hydrogen bonding between amino silane and silica surface. After drying particles are resuspended in PBS (pH 7.4) to a concentration of 1.56mg/ml.

3.1.3 Iron Oxide Attachment

15nm Carboxylate modified Iron Oxide NPs were purchased from Ocean Nanotech. Iron oxide NPs are attached to amine modified silica surface in a two-step process – (1), they are electrostatically attracted to the Janus template surface and then (2) covalently attached by amide linkages. 500uL of amine modified Janus templates are added to 3.5mL of PBS and 10ul of 5mg Fe/ml COOH-IO and stirred for 20 minutes. After initial electrostatic attachment, excess iron oxide is removed by centrifugation at 3221g for 5minutes. The pellet was resuspended in 100uL EDC (0.0019mg/ml in 0.1M MES; 1-ethyl-3-(3-dimethylaminopropyl)carbodiimide), 105.5uL NHS (0.0027mg/ml in 0.1M MES; N-Hydroxysuccinimide) and 4mL PBS and stirred for 20 minutes[77]. The reaction mixture was then centrifuged at 3221g for 5 minutes.

3.1.3.1 Blocking

Activated domains of IONP consist of an NHS-ester on its surface (Figure 4.3b). To minimize crosslinking, this domain can be hydrolyzed by increasing the pH >8, leaving behind the original carboxylic acid surface (Figure 4.3c). This was done by resuspending pellet from 3.1.3 in PBS-NaOH (pH 8.3-9) followed by washing in DI water. Alternatively, the NHS ester can be stopped from reacting with aminated Janus template surface by introducing a competing molecule (Figure 4.3d). This was done by resuspending pellet in 50mM Tris HCl (pH 8.3-9) followed by three washes in DI water. Blocking with Tris HCl leaves a surface of hydroxyls on IONPs. For subsequent steps, it is necessary that salts are removed from this reaction thoroughly by sonicating between washing steps and changing tubes whenever possible.

3.1.4 Silica Shell Formation

As in 3.1.1 silica is grown by the St**o**ber's process: particles from 3.1.3 (after blocking and washing) are added in a polymerization mixture along with TEOS. Polymerization mixture consists of 700uL DI water, 2mL IPA and 1.3mL NH_4OH. Iron oxide modified Janus templates suspended in 1mL IPA are added to the polymerization mixture and allowed to stir for a few minutes. After this, silica precursor is added dropwise during sonication in a bath at 42kHz. The

reaction is allowed to sonicate for total of 10 minutes after which it is stirred for 50 minutes at room temperature. TEOS is diluted in IPA (1.4uL/1mL (v/v) TEOS/IPA) and dropwise addition is done at an approximate rate of 1ml/min. After 50 minutes, particles are centrifuged at 3221g for 5 minutes and washed in EtOH.

3.1.5 Polystyrene Etch

Polystyrene portion of the Janus template is etched to create a payload loading domain for future endeavors. This final particle morphology is hereafter referred to as *nanobowl (NB)*. For this, particles from 3.1.4 are resuspended in 5mL Dimethyl Formamide (DMF; Sigma Aldrich), transferred to a glass vial and stirred at 60°C overnight. The next day, particles are washed in EtOH by centrifugation and dried in a vacuum oven to determine yield.

3.1.5.1 Fluorescent Labeling of Particles

Fluorescent particles were used for accumulation experiments. For this, 20uL of FIT-C-APTES (FIT-C: Fluorescein Isothiocyanate) silane conjugate was added at the same time as polystyrene etch.

3.1.6 FIT-C-APTES Silane Conjugate

In 5mL of EtOH, ~15mg FIT-C and 100ul APTES were added and stirred overnight[78]. Every time before addition to DMF mixture for labelling, the FITC-APTES was filtered through a 0.22um (EMD Millipore) filter to remove aggregates formed due to polymerization of silanes.

3.1.7 PEG Silane Surface Functionalization

Silica surfaces of Janus templates or Iron-oxide-silica composites from step (E) in Figure 4.3 can be coated with a PEG silane to enhance colloidal stability and reduce non-specific adhesion. For this, 0.9mg of PEG5kDa-silane (LysanBio) was suspended in 4mL EtOH and added to 0.78mg particles, sonicated and stirred overnight at 60°C. The next day, particles were washed in EtOH three times and dried in a vacuum oven as in step 3.1.2.

3.2 Particle Characterization

3.2.1 SEM, TEM

Particles were imaged on a Zeiss Sigma 500 SEM for morphology and aggregation studies. Backscatter was used for imaging composite surfaces like silica and iron oxide. JEM-1400 Plus Electron Microscope TEM was used for imaging iron oxide nanoparticles. Samples were prepared on aluminum (SEM) or copper grids (TEM) by drop casting and drying.

3.2.1.1 Iron Oxide NP counts per NB

SEM images were used to count Iron oxide NPs per nanobowl on ImageJ software[79]. At least 10 Janus templates were analyzed per image and results are displayed as an average over several preparations. Iron oxide NPs on one face were counted and multiplied by 2 to give the total number per Janus template. Iron oxide NPs only on one hemisphere of the template were counted (the other side is accounted for at the time of multiplication).

3.2.2 Size Distribution and Colloidal Stability

Malvern Instruments Zetasizer Nano was used for Dynamic Light Scattering measurements. Number and Intensity distributions were used for characterizing size distributions. Stern potential was measured as the Zeta potential. For stability analysis, time dependent size and zeta potential curves were obtained over the course of four days.

3.2.3 Magnetic Measurements

An MPMS3 SQUID magnetometer from Quantum Design was used for magnetic measurements. For zero field cooling (ZFC), sample was cooled down to 5K without a field and the magnetization was recorded at 100Oe as temperature increased. Field cooling (FC) measurements were done at 100Oe with reducing temperature. Liquid samples were suspended in water and sealed in a quartz tube.

(a)Diamagnetic correction for MvsH curves: Diamagnetic corrections were made according to Bain et.al.[80] (b)Diamagnetic correction for ZFC/FC: Magnetic moment at 5K on the ZFC curve was assumed to be solely from diamagnetism. Diamagnetic susceptibility is

independent of temperature and corresponding moment was subtracted from raw moment at all temperatures.

Langevin Fits from equation 2.24 were used to fit M vs H data to estimate magnetic diameter. Saturation magnetization was fixed as that measured experimentally and magnetic moment per particle (*m)* was determined from the fit. $m = V_m M_{spot}$ where M_{spot} is the spontaneous magnetization (for magnetite = 305kA/m[81]). Radius was determined from magnetic volume V_m.

3.2.4 Inductively Coupled Plasma- Mass Spectrometry (ICP-MS)

Nanobowls were digested separately in nitric acid and 10M NaOH for iron and silica digestion respectively. For this, an unknown amount was microwaved with digestion buffer at 150°C for 20 minutes and then 215°C for 10 minutes. After cool down, digestion vessels were washed with DI water and run through a Thermo iCAP RQ ICP-MS.

3.3 Magnetic Drift Velocity

3.3.1 NP Accumulation in a Magnetic Field Gradient

Nanoparticle magnetic drift velocity ($\vec{v}$) was determined from the mass transfer toward a NdFeB magnet. For this purpose, the rate of change of concentration with time was measured at two locations in a PDMS well: (1) location closest to magnet where *accumulation* occurs (2) location furthest from magnet where particles *drain* from. $\vec{v}$ was determined from Fick's second law[82,83]:

$$\frac{dc}{dt} = -\nabla.\vec{J} \quad (3.1)$$

$$\vec{J} = \vec{v}c \quad (3.2)$$

$$\frac{dc}{dt} = -c(\nabla.\vec{v}) \quad (3.3)$$

Where J is the advective flux, and c is the concentration. Reducing to a 2D problem with two equal dimensions and assuming that the velocity in all directions is the same, the above equation can be written as[84]:

$\frac{dc}{dt} = -2\frac{d\vec{v}c}{dx}$; dx = length of well (3.4)

To measure concentration at either location, absorbance (non-fluorescent particles) or fluorescence was measured on a Tecan Infinite Pro Spectrometer. Concentration for calculations was relative to the total at any time point. For this spectrometer reading at each location was divided by total amount of particles measured for that time point.

Particles in a 14mm PDMS well (Figure 3.2a) were exposed to a 0.48T magnet at a distance of 0.5cm. The field was 0.18T and the magnetic field gradient was 0.269T/cm. 50uL of particles were collected at selected time intervals from three locations in the well: (A) 5mm from magnet (edge of well near magnet)- where *accumulation* occurred, (B) 19mm from magnet (farthest edge from magnet)- where particles *drained* from, (C) center of well. Absorbance for non-fluorescent samples was measured at 450nm and fluorescence (FIT-C) at ex/em: 490/535nm. Nanobowls were filtered through a 0.45um filter to isolate particles less than the pore size.

As a control sample, 3um-12um amine modified iron oxide nanoparticles were used. They were sonicated in a bath for 14 minutes to yield ~ 60nm nanoparticles and then separated through 0.45um filter. Control sample measurements were repeated atleast three times and three different batches of nanobowls were tested.

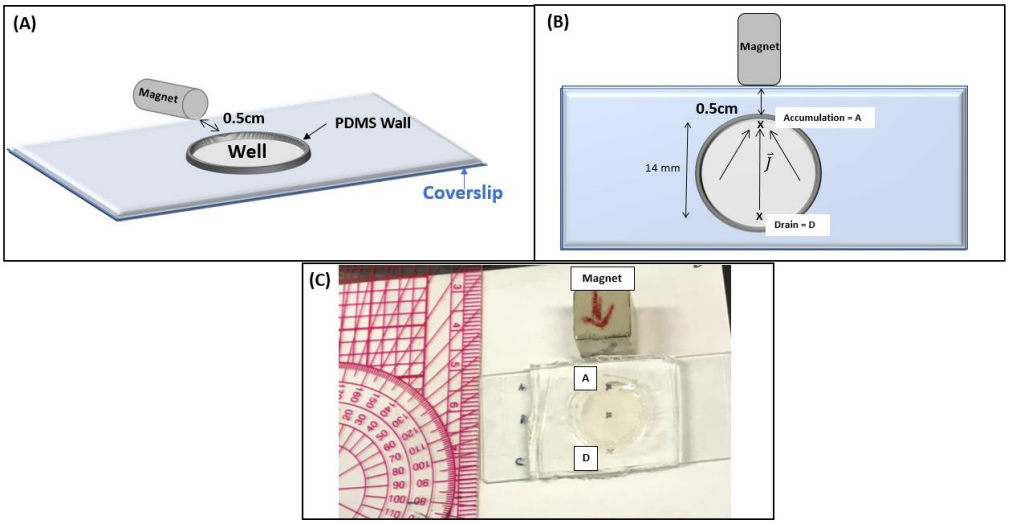

Figure 3.1: (A) Schematic of set-up for accumulation in a magnetic field gradient. (B) Dimensions of well and distance from magnet. A, B & C correspond to locations where samples were collected from. (C) Image of experimental set-up.

3.4 Imaging nanobowls on Optical Microscope

Nanobowls for this study were used as synthesized without size exclusion. A 5mL syringe was loaded with ~$10^8 particles/mL$ and 0.5mL was pushed through a microfluidic channel (300μm x 300 μm square channel, Figure 3.3a, b). The channel was cast in PDMS and adhered to No0. Thickness cover slip by UV-ozone activation followed by heating at 80°C. Syringe was connected to chip with 0.05 inch Tygon tubing from Cole Palmer. For determining magnetic drift velocity, syringe inlet, chip and outlet were kept at the same height ~30cm from ground (Figure 3.3c). A 0.5 x 0.5 inch cube N52 magnet was kept 1cm from channel. For particle trajectories in 15um/s convection, the height difference between the inlet and chip was 30cm and flow occurred by siphoning (Figure 3.3d). The magnet was kept at 1cm and 0.5cm from the channel. Images were taking in brightfield at a 160X magnification on Olympus inverted microscope. Frame rate was adjusted for each experiment for maximum pixel and trajectory resolution, it was between 540ms/frame -650ms/frame. The field of view was 92x 92um. Magnetic Field was measured on AlphaLab DC Gaussmeter M1ST and gradients were determined from the local slope of the line (Figure 3.3e).

Images were processed in MATLAB for determining net distance travelled between several frames. After contrast enhancement and background subtraction, several frames of particles were processed using Simple Tracker[85] functions that tracks particles across several frames. Pixels were calibrated to distance using a microscope scale. Images were sectioned so that only there was only one particle per frame. Image region properties were used to determine particle centroid diameters. Number of particles in each cluster were determined by dividing measured diameters by average diameter on SEM.

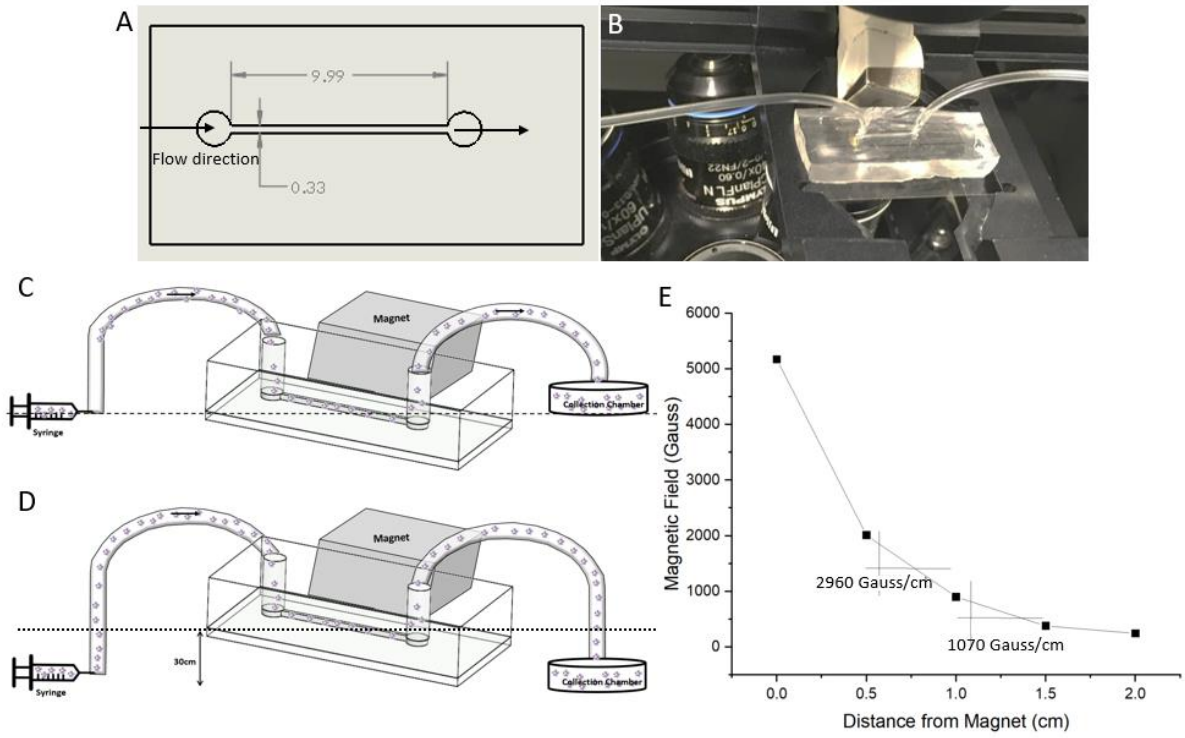

Figure 3.2: (a) Dimensions of channel. (b) Microfluidic chip set-up. Schematic of set-up for (c) magnetic drift velocity determination, (d) particle trajectories in convection. (e) Magnetic field of N52 magnet.

Chapter 4

Characterization of Magnetic Nanobowls

4.1 Synthesis of Magnetic Nanobowls

4.1.1 Layer-by-Layer Assembly

Magnetic Nanobowls are synthesized in a layer-by-layer fashion on a silica template[11] as shown in Figure 4.1. Particle synthesis is optimized for aggregation and stability and also addresses some concerns regarding toxicity due to iron oxide overload in cells[86,87]. First, polystyrene (PS) spheres and a silica precursor are reacted to produce silica-PS Janus template (Figure 4.1b). Nucleates from polymerization of the silica precursor[88] (TEOS) undergo collisions with the PS spheres in solution. The interaction of nucleates with PS is controlled by diffusion through the double layer of PS spheres, therefore different morphologies are achieved depending on the surface charge on PS spheres[74]. Amine, hydroxyl and sulphate coated PS spheres result in the complete formation of a silica shell, while carboxyl- PS gave bowl like Janus templates. The size of the bowl may be controlled by limiting the concentration of the silica precursor or reaction time[88]. The morphology of Janus templates synthesized with PS-COOH and silica have been shown to depend on the diameter of PS-COOH core and silica nucleates – larger the silica nucleate size, the more likely a bowl like conformation. Smaller silica nucleates result in progressively bumpier raspberry like structures[75].

Following synthesis of a Janus template, its silica surface is modified with an amine-silane to which iron oxide nanoparticles are attached via amide linkages (Figure 4.1d). In order to minimize oxidative stress related toxicity in cells, magnetic particles are coated with a silica shell. PS sphere is etched away to give nanobowls (Figure 4.1f) that have a cavity for drug loading post-processing.

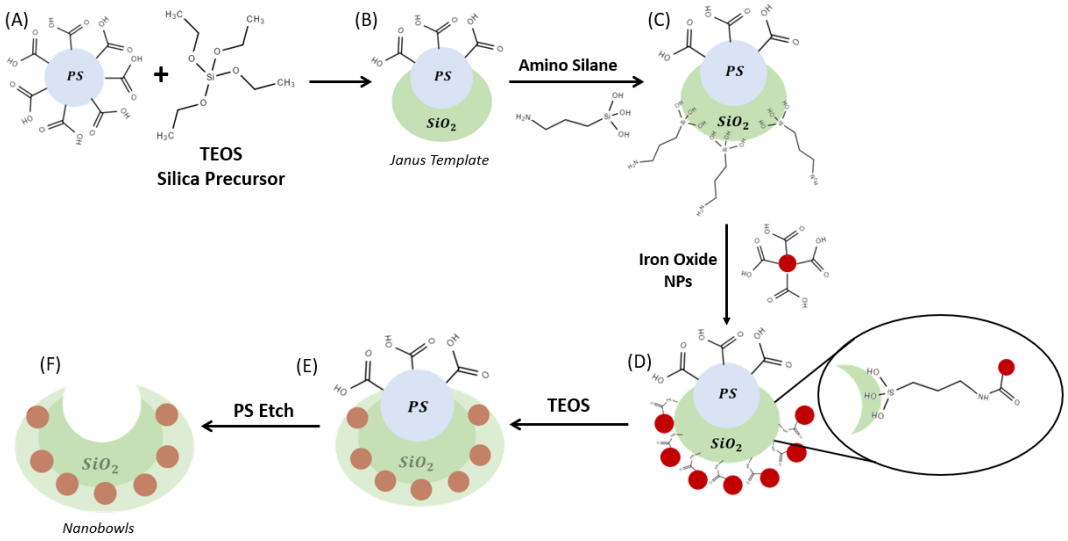

Figure 4.1: Schematic of Layer-by-layer synthesis of Silica-Iron oxide Nanobowls

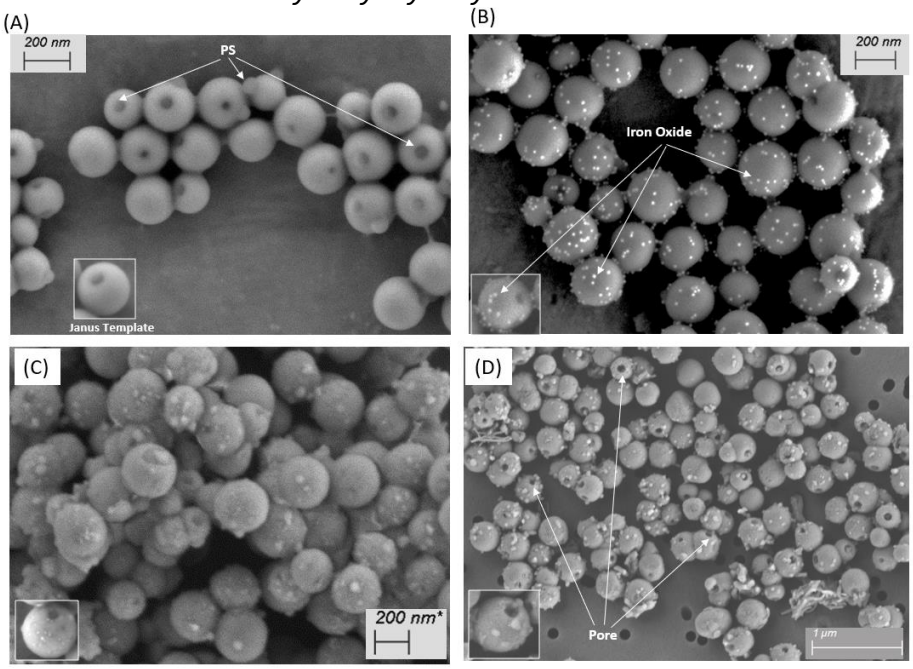

Figure 4.2: SEM images of layer-by-layer synthesis of Nanobowls. (A) Amine modified Janus template. (B) Iron oxide attachment on Janus template. (C) Magnetic Janus templated coated with silica shell. (D) Magnetic nanobowls with PS etched away on 200µm pore filter paper membrane.

4.1.2 Aggregation and Crosslinking

Maintaining kinetic independence of nanoparticles is important for fine tuning magnetic and fluidic properties. As seen in Figure 2.10, both magnetic force and Stokes drag vary with magnetic radius and particle radius, respectively. Therefore, flocculation could lead to a suspension with inhomogeneous magnetic properties, unideal for establishing precise control over drug delivery. The smallest blood vessels in the human body are 3-4um in diameter: capillaries supplying bronchioles in lungs are on average 6.3um in diameter[89] and cerebral capillaries range from 2-5um. Aggregates of flocculated particles can also lead to clogging of blood vessels during *in vivo* delivery. Additionally, particles must have mechanical durability to withstand physiological flows with Reynold's number up to 4500[48] and shear stress up to 4.5Pa[90]. To this end, several steps have been taken to minimize aggregation and increase mechanical durability.

Aggregation in this layer-by-layer approach may occur due to polymer bridging or crosslinking. In order to minimize aggregation by polymer bridging, short chain silanes have been used to modify the Janus template silica surface with amines in step (C) (Figure 4.1). Crosslinking may occur in the subsequent step where spherical iron oxide nanoparticles act as crosslinking agents by binding to two Janus templates (Figure 4.3a). This is avoided by deactivating iron oxide or blocking its activated domains as described in section 3.1.3.1. Figure 4.4(A) shows that the polydispersity in samples before (width of curve 825nm) and after amine modification (width of curve 800nm) is similar, indicating that aggregation has not occurred. Figure 4.4(B) shows an instance of crosslinking when double the number of crosslinking agents (EDC, NHS) are used for attachment. It appears that several Janus templates become linked in a network via the iron oxide NPs attached on them. Upon deactivation or blocking as in Figure 4.4(C) and (D), crosslinking is significantly reduced but there is greater heterogeneity in the number of iron oxide NPs per Janus template – from a 40% variability in the crosslinked sample versus ~60% for blocked samples. However, nanobowls can be separated based on their

magnetic strengths by attracting them to a magnet for given times based on their magnetic drift velocities.

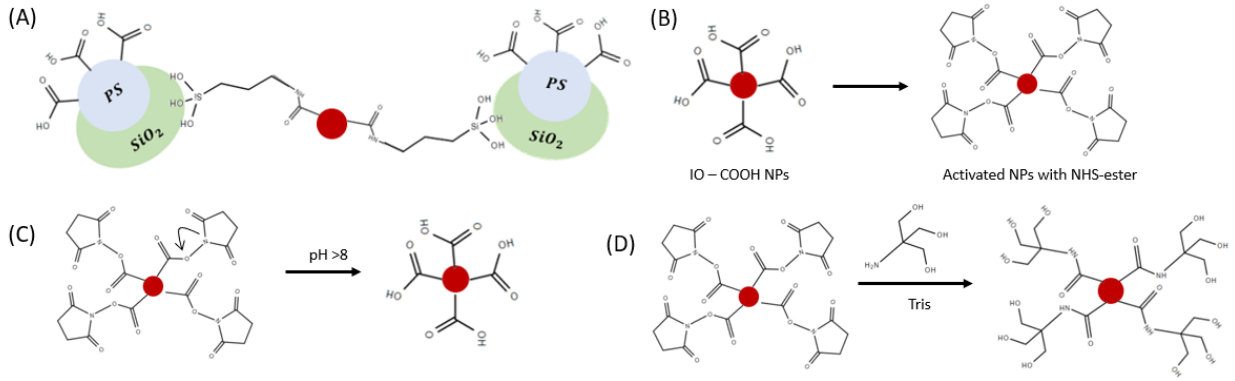

Figure 4.3: Schematic of blocking strategies. (A) Crosslinking via amide linkages to iron oxide NP; (B) NHS-ester activated domain of Iron oxide NPs; (C) Hydrolysis of NHS-ester; (D) Tris HCl blocking.

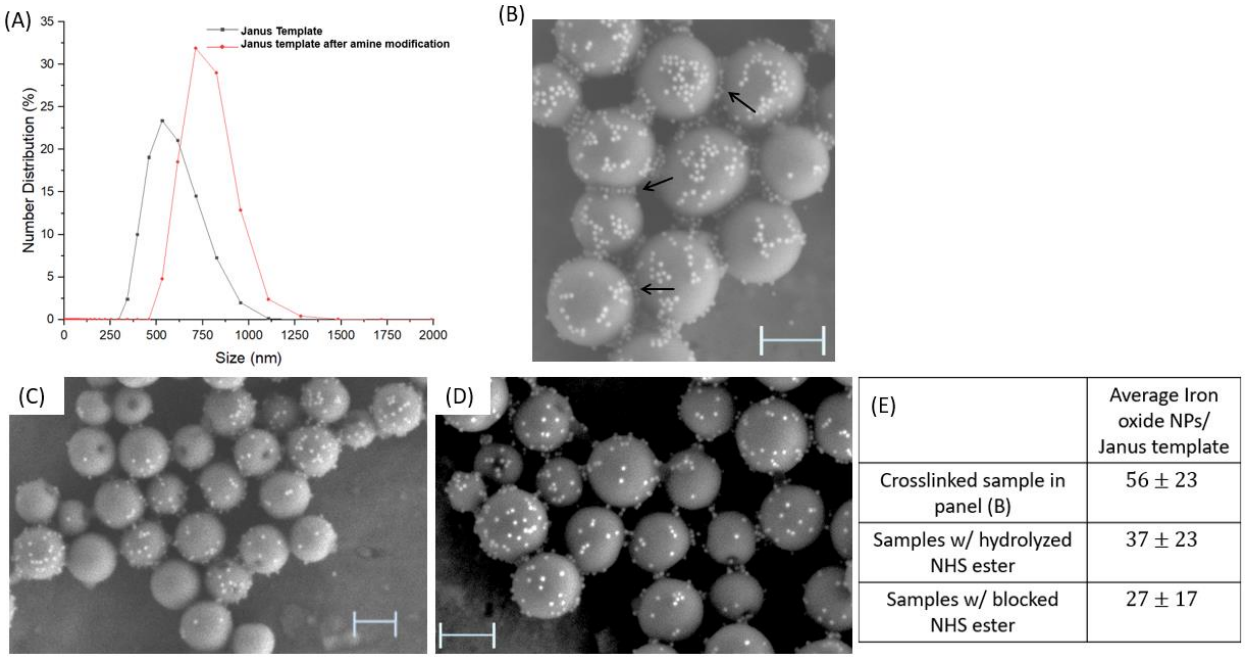

(E)	Average Iron oxide NPs/ Janus template
Crosslinked sample in panel (B)	56 ± 23
Samples w/ hydrolyzed NHS ester	37 ± 23
Samples w/ blocked NHS ester	27 ± 17

Figure 4.4: (A) DLS size distributions of Janus templates before and after amine modification. (B) An instance of crosslinking (black arrows). Iron oxide modified Janus templates deactivated by (C) hydrolysis of NHS ester and (D) Tris HCl blocking. (E) Iron oxide per template counts. All scale bars are 200nm.

Mechanical durability is ensured by using covalent linkages at each step. An amino silane binds to the Janus template via siloxane bonds. Iron oxide nanoparticles form amide

bonds with amine modified Janus templates and in the last step, the silica layer forms siloxane bonds with the underlying Janus template. It is seen that iron oxide NPs are able to stay attached to the Janus template over the course of seven days at 4°C despite spinning at 3221g once each day (Figure 4.5). Iron oxide NPs per Janus template are 39 ± 13 (n = 13) for day 1 and 42 ± 14 (n=15) for day 7. A p-value of 0.564 is obtained from student's t-test for these samples, suggesting that statistically, they are not different from each other.

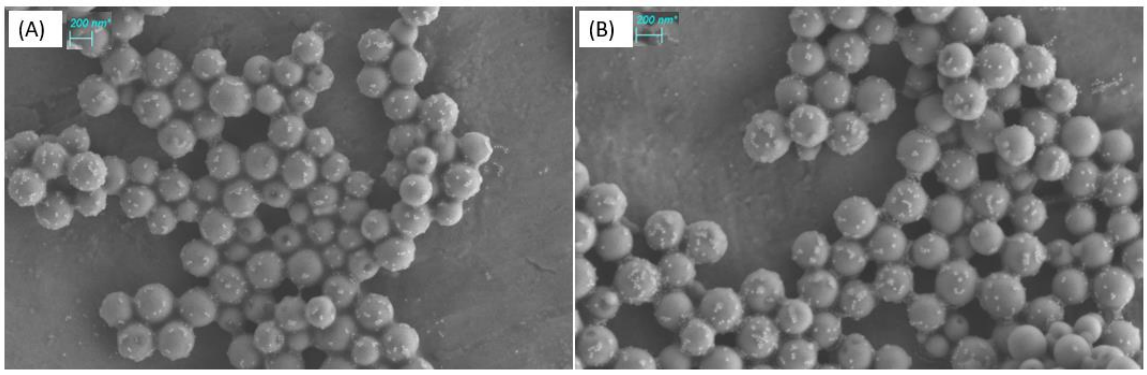

Figure 4.5: Iron oxide modified Janus templates at (a) day 1, (b) day 7.

4.1.3 Iron Oxide Attachment

Iron oxide nanoparticles (IONPs) were confirmed to be $15 \pm 2nm$ from TEM images (Figure 4.6) and there is a 4nm thick organic layer on their surface by the manufactures specifications. DLS data showed that their average hydrodynamic diameter was ~44nm and zeta potential -43mV (Figure 4.6). It also indicated the presence of aggregated particles in solution (broad asymmetric peak in Figure 4.6c) Two methods of iron oxide attachment were explored: (1) functional group (COOH on Iron oxide NP) activation and covalent attachment, (2) electrostatic attraction to template followed by functional group activation and covalent attachment. As can be seen in Figure 4.7(a), very few Iron oxide NPs (IONP) are attached to Janus templates when their activated form is mixed with Janus templates. This may be because bulky NHS ester rings cause IONP-IONP repulsion. Janus templates have a positive surface potential confirmed by a Zeta potential of ~20mV attributed to the aminosilane layer on their surface. Opposite surface potentials of IONPs and Janus templates has been leveraged to

attract a larger number of IONPs to the template surface (Figure 4.7(b)). Subsequently, the crosslinking molecules (EDC and NHS) were added to initiate covalent binding of attracted IONPs (Figure 4.7(c)).

The number of IONPs per Janus template has been quantified before the covering with a silica shell by counting IONPs in SEM images. Figure 4.7(d) shows that there is a fair amount of polydispersity in terms of IONPs/Nanobowl with an average of 56 ± 17. This average from the counting method gives an Fe:Si ratio of 0.00285. It is confirmed by ICP-MS analysis for nanobowls after silica shell growth and PS dissolution to be 0.00338. This is within 20% of the estimate received from counting, indicating that loss of IONPs during silica shell growth is minimal. Although several measures were taken to make the counting method accurate and informative, it is noteworthy to point out that one major assumption made was that IONPs are homogenously distributed around the template and both hemispheres will have the exact same number of IONPs.

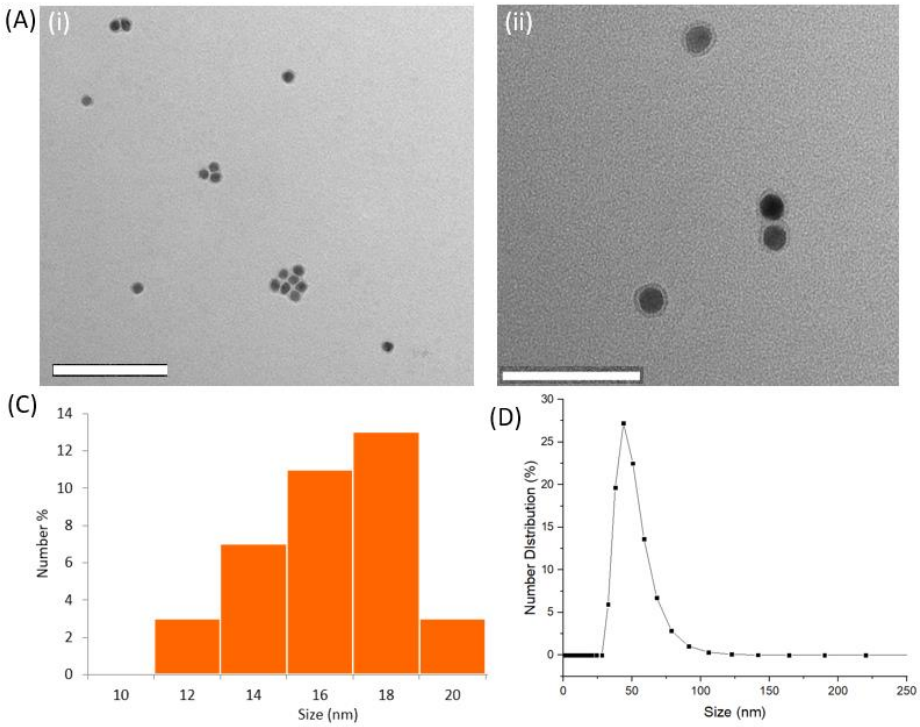

Figure 4.6: (a) TEM image of 15nm IONPs. (i) scale bar 200nm; (ii) scale bar 100nm. (b) Size distribution histogram of IO core from TEM images. (c) DLS size distribution.

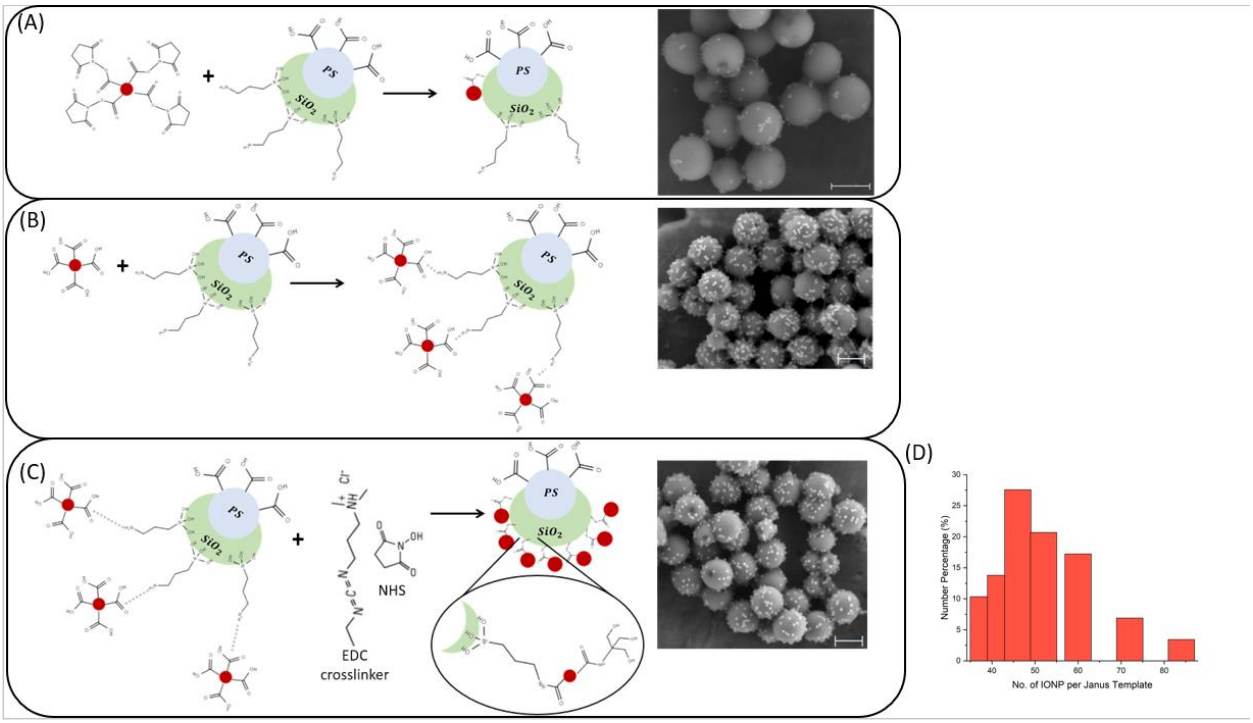

Figure 4.7: Iron Oxide NP attachment to Janus Template. (a) Covalent attachment of activated Iron oxide NPs. (b) Electrostatic attachment of Iron oxide NPs followed by (c) covalent attachment. (d) Number percentage of Iron oxide NPs per Janus template for all nanoparticle preparations used in this study. All scale bars are 200nm.

4.1.4 Silica Shell Formation

The purpose of forming a silica shell is to minimize toxic effects of iron oxide on cells. Therefore, it is imperative that the surface of iron oxide particles is fully covered with a silica layer. Both blocked and deactivated IONP modified Janus templates were coated with silica. It was observed that silica covered iron oxide in Tris HCl blocked samples but not in PBS deactivated samples. Backscattering of electrons from a surface depends on the mass of their nuclei and can be used to distinguish heavier atoms from lighter ones based on intensity. Heavier nuclei backscatter electrons more efficiently and appear brighter in a SEM – Backscatter Electron Detector (BSED) image. Figure 4.8 shows secondary electron (SE) and corresponding BSED images of bare IONP modified Janus templates and silica coated nanobowls. It can be seen that bright spots of iron oxide are more prominent in bare IONP-Janus templates and PBS deactivated silica coated nanobowls. This is quantified by the rate of

change of intensity along a line on a nanoparticle (Figure 4.8h). Tris HCl blocked silica coated nanobowls show a relatively flat intensity profile and spikes in rate of change of intensity that are almost four times smaller than bare IONP Janus templates. Contrastingly, PBS deactivated silica coated nanobowls have a rate of change of intensity on the same order of magnitude as bare IONP Janus templates indicating that these particles contain iron oxide that is not completely coated with a silica shell. A likely explanation may be that after deactivation with pH>8, the exposed surface of IONP is composed of carboxyl groups that electrostatically repel silica nuclei. On the other hand, Tris HCl blocking leaves IONP surface with hydroxyl groups that can form hydrogen bonds with silica nuclei allowing for full coverage. Further, to confirm that IONPs were not lost in Tris HCl blocked samples, EDS (Energy Dispersive X-ray Spectroscopy) was used. As can be seen in Figure 4.9, both spectra for before and after silica coating overlay each other fairly well suggesting that approximately the same amount of Iron and silica are present in both samples.

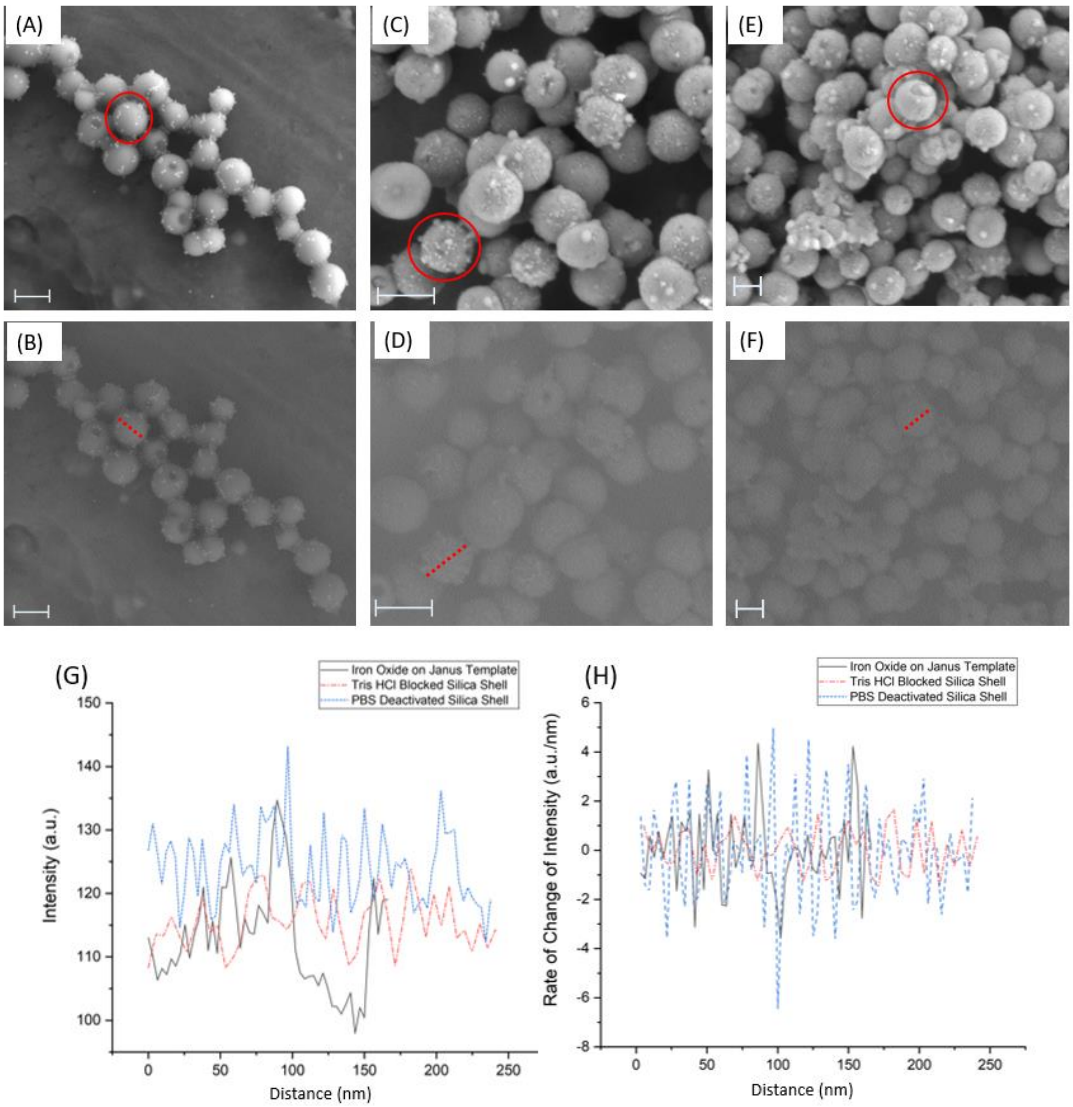

Figure 4.8: (a, b) Bare IONP modified Janus Templates (scale bar: 200nm). (c, d) PBS deactivated silica coated nanobowls (scale bar: 300nm). (e, f) Tris HCl blocked silica coated nanobowls (scale bar: 200nm). A, C, E: SE images. B, D, F: BSED images. (g) Intensity profile over a 1D region on a nanoparticle. (h) Rate of change of intensity over that said region. (Nanoparticles and regions analyzed in (g) &(h) are marked in red).

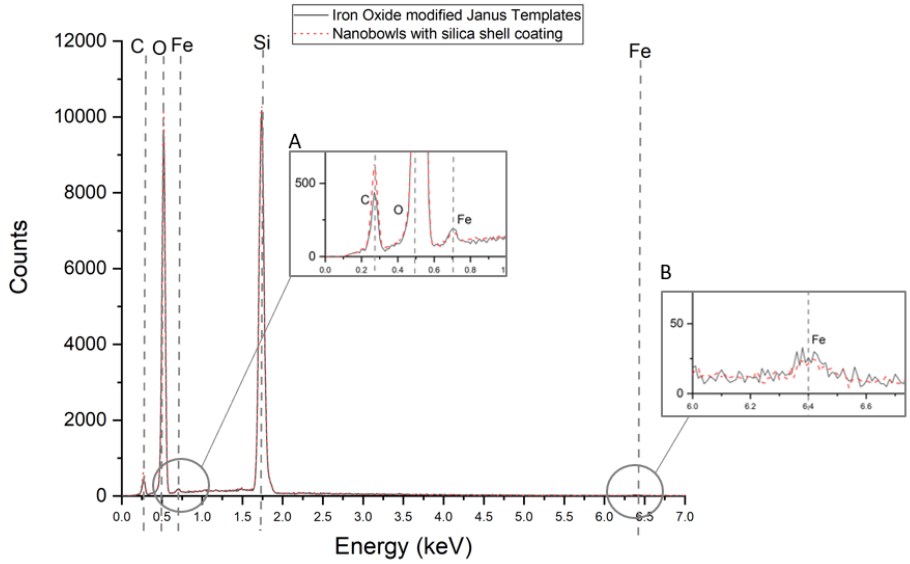

Figure 4.9: Energy Dispersive X-ray Spectrum for IONP modified Janus templates and Tris HCl blocked silica coated nanobowls. Insets: Zoomed in (A) Lα (B) Kα peak of Iron.

4.2 Colloidal Stability of Magnetic Nanobowls

Nanobowl stability has been analyzed using zeta potential and time dependent size distributions. A single nanobowl has an average diameter of 210-300nm (Figure 4.10a) found from SEM images. The initial synthesis appears to contain larger clusters of nanobowls as seen in the wide peak that extends from 200-1000nm in Figure 4.10b. These larger particles are removed by pushing the suspension through a 0.45um filter, although smaller particles from the filter membrane may leak through to contaminate the nanobowl suspension. Nanobowls have a zeta potential of ~23mV – resulting DLVO energy potential curves with a secondary minimum indicating that they are stable over a short amount of time. Zeta potential begins to drop after storage in 4℃ for three days (Figure 4.10d) causing increased flocculation as seen in the widening peak for Day 4 sample in Figure 4.10b. Nanobowls can also be modified with PEG for increasing biocompatibility for *in vivo* applications. Coating with a 5kDa PEG-silane lends similar stability as bare nanobowls (Figure 4.10e) although giving lower zeta potential of 8mV. PEG-coated nanoparticles are known for enhanced biocompatibility due to the ability to minimize adsorption of proteins on the NP surface due to steric repulsion[30].

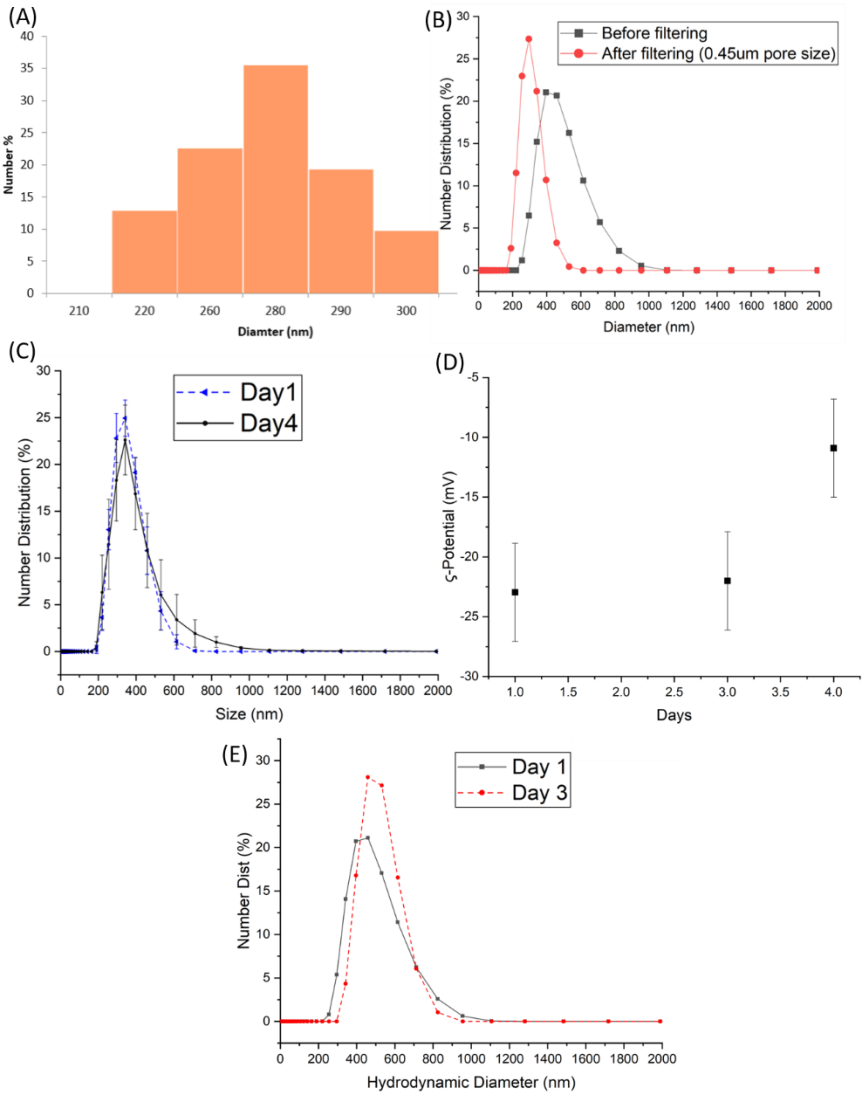

Figure 4.10: (a) Histogram of nanobowl size measured from SEM images for all preparations used in the study. (b) Size distributions of a nanobowl preparation before and after filtering. (c) Average size distributions of nanobowls for all preparations used. (d) Time dependent zeta potential of nanobowls. (e) Size distributions of PEG coated nanobowls over three days.

4.3 Magnetic Properties of Nanobowls

4.3.1 Magnetic Measurements

(a) Magnetization vs Field Measurements

IONPs show saturation magnetization (M_s) of ~85emu/g that is close the bulk saturation of magnetite (Fe_3O_4) ~95emu/g, however, M_s of iron oxide in nanobowls is only ~40emu/g. This decrease in magnetization may indicate the oxidation of some or all of the magnetite in IONPs

to lower magnetization phase (M_s=75emu/g) of maghemite ($\gamma - Fe_2O_3$). Magnetite is a metastable phase of iron oxide that spontaneously oxidizes to maghemite in air over long periods of time. Oxidation can also be induced by pH of the solution- basic environments may lead to electronic transfer such that Fe^{3+} ions are incorporated in the particle,[59,91] a likely possibility in our case as all modification steps were in 7<pH<10.

One way to identify the difference between magnetite and maghemite is the Verwey transition in magnetite. At around 125K (T_v, bulk) magnetite's crystal structure changes from monoclinic to cubic spinel – a high anisotropy phase to smaller anisotropy at higher temperatures[92]. It can be seen that the anisotropy field of both, IONPs and nanobowls, increases with temperature: 1000 Oe at 300K to 2000 Oe at 5K. It is therefore unlikely that magnetite was oxidized to maghemite. However, magnetic measurements leave us with inconclusive results on this front. Further studies with X-ray photoelectron spectroscopy (XPS or Mössbauer spectroscopy are needed.

It is important to note that despite the M_s of nanobowls being less than that of IONPs, there is greater magnetic force acting on them (for a fixed field gradient). Magnetic force is a function of magnetic moment which depends on magnetization and magnetic volume. Due to ~50 times more magnetic volume, magnetic moment of nanobowls is 25 times that of IONPs. Therefore, the greater magnetic volume in nanobowls is able to off-set the decrease in per particle magnetization resulting in greater magnetic force acting on them.

(b) ZFC-FC Measurements

ZFC and FC measurements were done in an aqueous solution wherein moment alignment can only occur by Neèl relaxation at temperatures below 273K due to freezing of water. Magnetization on the ZFC curve (Figure 4.11 (c)) for IONPs increases with temperature as thermal energy allows more moments to align with applied field. The curve begins to flatten as maximum magnetization at 100Oe is reached and the measurement time is at the same order of magnitude as the relaxation time. There is a steep increase in magnetization at 273K

as water begins to melt allowing physical rotation of particles. Relaxation occurs by rotation and moment flipping after melting for IONPs. In Table 4.1: $\tau_B < \tau_N \, and \, \tau_B < \tau_M$, where τ_M is the measuring time ~ $10^1 - 10^2 \, s$ for DC measurements[59]. Relaxation by both mechanisms is also the reason for aqueous solutions showing higher magnetizations than powders (Figure 4.11 (e) and (f)).

As the temperature continues to increase, magnetization begins to drop as thermal energy causes moments to flip faster than the measuring time. Nanobowls show a similar trend in ZFC curves (Figure 4.11 (b) and (c)), however the steep increase in magnetization at 273K is less pronounced. This may be attributed to the increased Brown relaxation time ($10^{-2} s$) due to larger magnetic radius of nanobowls: Another plausible explanation is that particles are unable to rotate to align with the field due to high anisotropy.

All samples share common features like broad peaks and high blocking temperatures This can be attributed to the large diameter of nanoparticles and large size distributions[93]. The distribution of IONPs on each nanobowl is fairly large with a standard deviation of 30% and IONPs showed an aggregation in DLS measurements. Additionally, moments get blocked around 250K, indicating high thermal irreversibility of FC. This can be because of two reasons: (1) high anisotropy caused by inter-particle interactions or (2) canting of surface spins[93].

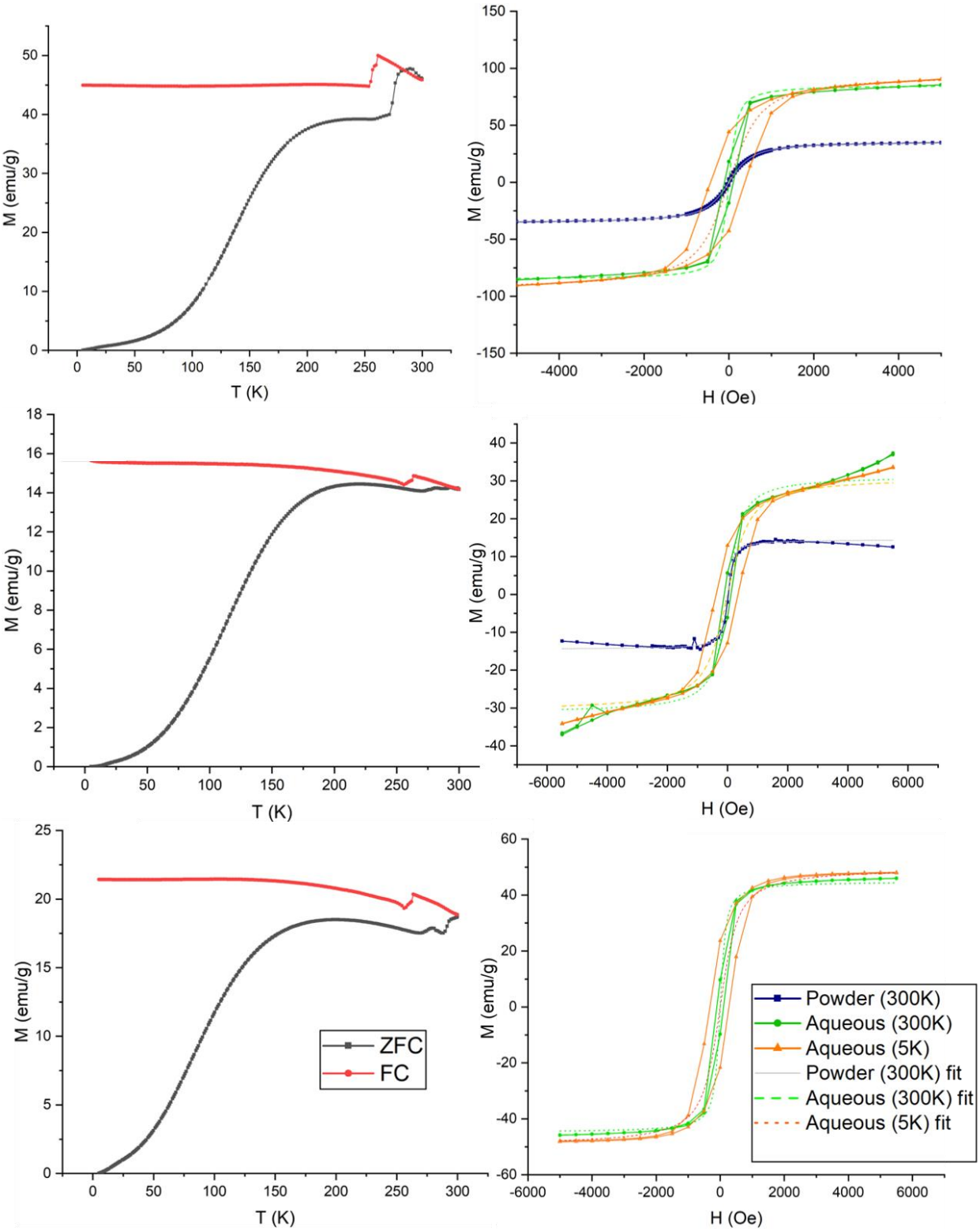

Figure 4.11: ZFC and FC curves of (a) 15nm IONPs (b), (c) Nanobowl samples. Magnetization curves for (e) 15nm IONPs (f), (g) Nanobowl samples corresponding to plots in a, b, and c respectively.

Table 4.1: Magnetic Parameters from magnetization data in Figure 4.11 and its fits.

	Magnetic radius EM (nm)	Magnetic radius Langevin fit (nm)	Hc (Oe)	Ha (Oe)	Ku (J/m^3)	Neel relaxation (s)	Brown relaxation (s)	Ms (emu/g)	Ms Langevin fit (emu/g)	Mr (emu/g)	Volume (magnetic) (m^3)	Volume (hydrodynamic) (m^3)
15nm Iron oxide powder (300K)	15 ± 2	5.1 ± 1.2	25	2000	$2x10^4$	$7x10^{-6}$	$6x10^{-6}$	38.9	35.8436	2.7	$2\ x\ 10^{-24}$	$2\ x\ 10^{-24}$
15nm Iron oxide aqueous (300K)		7.3 ± 6.9	100	1000	$2x10^4$	$2x10^{-5}$	$2x10^{-5}$	85.5	85.5	18		$3.3\ x\ 10^{-24}$
15nm Iron oxide aqueous (5K)		4.6 ± 3.2	375	2000	$5x10^4$	2.23	$2x10^{-5}$	95.002	95	43		
15nm Iron oxide aqueous (300K)	Average moment (Am^2)							$8\ x\ 10^{-19}$				
Nanobowl Powder (300K)	29 ± 3 *	7.2 ± 3.6	29	1000	$4x10^3$	$9\ x\ 10^{30}$	$1x10^{-2}$	14.5	14.5	2.1	$1\ x\ 10^{-22}$	$1\ x\ 10^{-20}$
Nanobowl Aqueous (300K)		7.6 ± 5	100	1000	$1x10^4$	$8\ x\ 10^{116}$	$1x10^{-2}$	45.7	45	9.6		$2\ x\ 10^{-20}$
Nanobowl Aqueous (300K)		6.75 ± 9.6	125	1000	$1x10^4$	$3\ x\ 10^{87}$	$1x10^{-2}$	35	31	5.6		
Nanobowl Aqueous (5K)		5.3 ± 2.6	275	1500	$2x10^4$	$2\ x\ 10^{189}$	$1x10^{-2}$	48	48	21		
Nanobowl Aqueous (5K)		4.6 ± 2.4	350	2000	$2x10^4$	$7\ x\ 10^{172}$	$1x10^{-2}$	33	31	12.5		
Nanobowl Aqueous (300K)	Average moment (Am^2)							$2\ x\ 10^{-17}$				

*volume equivalent of 56 ± 17 IONPs/ nanoparticle. Hydrodynamic radius (r_H) for IONPs powder is the same as magnetic radius from EM. For nanobowls it is the radius of a nanobowl. For aqueous solutions, r_H is from DLS measurements.

4.3.2 Inter-particle Dipolar Interactions

Even complete oxidation of IONPs in nanobowls to maghemite does not explain the decrease in magnetization. Maghemite particles as small as 5-10nm have been reported to have $M_s$of 60-80emu/g[94–96], almost twice that we see in nanobowls. Another explanation for reduction in magnetization can be the demagnetizing effects of inter-particle dipolar interactions, evidence for which is also seen in ZFC curves. There are several features that identify these interactions in magnetic data – increased anisotropy, thermal irreversibility at high temperatures and increased blocking temperatures[55,97]. The applicability of these to nanobowls is discussed in the following section.

(a) Anisotropy and Particle Concentrations

Anisotropy coefficient K_u values have been estimated from equation 2.21 in Table 4.1. These are larger than bulk values for both magnetite ($1.35\ x10^4$Jm^{-3}) and maghemite ($4.6x10^3$ Jm^{-3}). This increase in IONPs' anisotropy can be due to surface canted spins or inter-particle interactions due to high particle concentration. Surface disordered spins are unlikely as this also leads to a reduction in magnetization from bulk value. Only a small reduction in magnetization is observed in our samples: Ms for IONPs = 85 emu/g as compared to 95 emu/g for bulk. This suggests that dipolar interactions due to a particle concentration of 10^{15} particles cm^{-3} (10% v/v) are be the cause of higher anisotropy constants. Goya et.al. reported similar increase in anisotropy in solutions with particle concentrations as low as 2% v/v [98]. Despite the concentration of IONPs in nanobowl suspension being several times smaller (0.01% v/v, 10^{13} particles cm^{-3}), K_u values are similar to those of 10^{15} particles cm^{-3} sample. This implies that IONPs on an individual nanobowl may be interacting due to a high per bowl spatial concentration of $5.6\ x\ 10^{15}\ \ particles\ cm^{-3}$ (3%v/v). The underestimation of magnetic radii from Langevin fits as compared to SEM and ICP-MS measurements can be also be attributed to this effect.

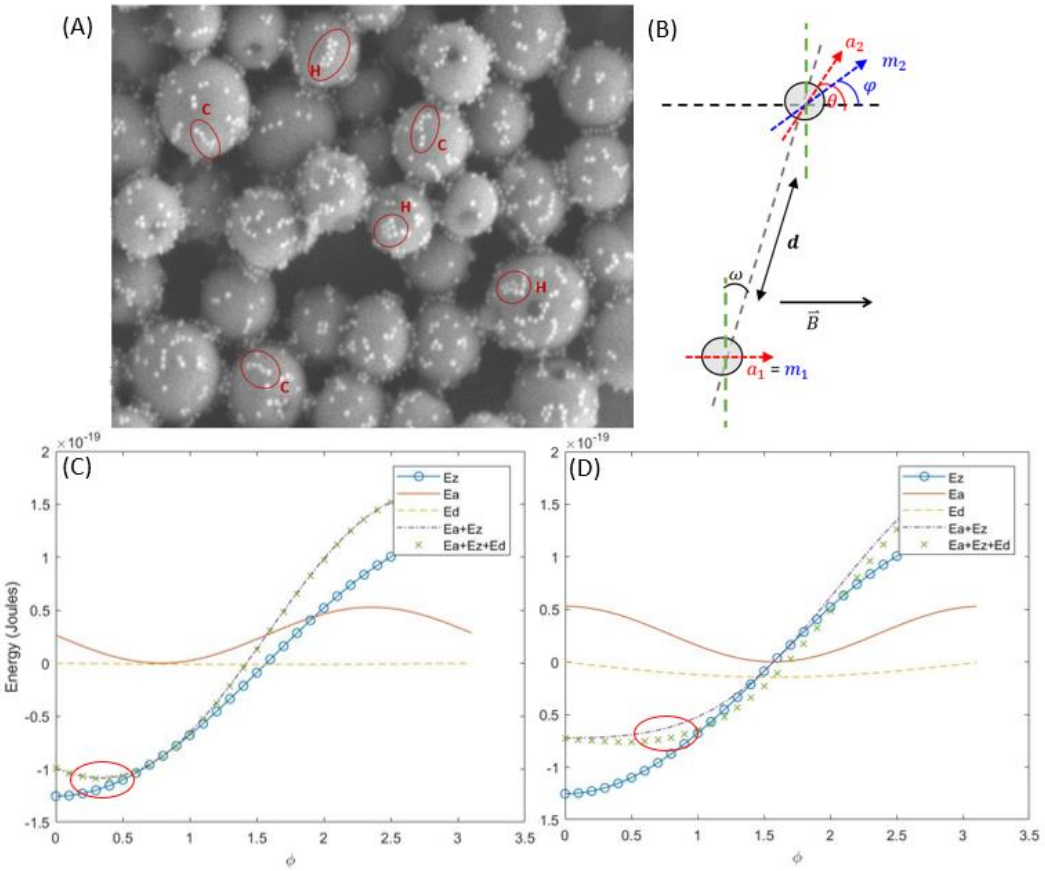

Figure 4.12: (a) Some IONP arrangements on nanobowls. C- chains, H- hexagonal arrays. (b) Schematic for axis and angles between two particles. a-anisotropy easy axis, m-magnetization, $\vec{B}$- applied field, d- inter-particle distance, angle between two particles =ω, $\vec{B}$ and easy axis =θ, magnetization and $\vec{B} = \phi$. (C) and (D) energy vs magnetization angle (ϕ) for different arrangements: (C) $\omega = 0°$, $\theta = 90°$, d = 20nm. (D) $\omega = 0°$, $\theta = 90°$, d = 0nm. (Angles in plots are in radians). Ea – anisotropy energy (Eqn 2.15), Ez- Zeeman energy (Eqn 2.16), Ed – dipole-dipole energy (Eqn 2.13).

(b) Dipole-dipole Interactions in Clustered Arrangements

Maximum magnetization is achieved when all moments are in the direction of the applied field. In nanobowls, this would mean that magnetization of all IONPs on the bowl should be in the direction of applied field. However, particle interactions prevent 100% alignment. Demagnetizing effect occurs when the magnetic field from one IONP effects the magnetization of another (dipole- dipole interactions) and prevents it from aligning with applied field. The strength of dipolar interactions depends on the inter-particle distance, orientation of easy axis and position of a particle with respect to those around it. Total energy potentials for two

interacting particles are plotted in Figure 4.12 using as the sum of anisotropic energy, Zeeman energy and dipole- dipole interactions (from equations 2.13, 2.15 and 2.16). Most probable magnetization angle can be found from the minimum of the total energy potential curve. In figure 4.12(d) dipole-dipole interactions shift the minimum energy from 0 (Ea+Ez curve) to 0.7 radians (40°, Ea+Ez+Ed curve) ($\omega = 0°$) when the inter-particle distance is smaller.

Previously, Klughertz et.al. have shown that the presence of random defects in 2D assemblies of nanoparticles with random easy axis orientations causes magnetic frustration and increases anisotropy. They showed that this was dependent on the number of defects and inter-particle distance[55]. Defects lead to the creation of magnetic domains that appear as clusters. Sanchez et.al. showed that the demagnetizing effect of dipolar interactions depends not only on inter-particle distance but also cluster shape and distance between them in random assemblies[54]. Upon studying SEM images of nanobowls, a vast heterogeneity in IONP arrangements is observed wherein they are deposited in randomly arranged clusters. Some IONPs are deposited as lone particles more than 30nm from any other, others are arranged in close-packed clusters like short chains and pyramidal arrangements in hexagonal arrays (Figure 4.12a). Due to their irregular arrangement on the silica template, some IONPs are within 10nm of each other. If all IONPs are assumed to be distributed evenly within the volume of a nanobowl, the mean inter-particle distance can be estimated to be 25nm. As inter-particle distance increases, dipolar interactions between particles decrease. At a distance of 20nm, dipolar interactions don't shift the magnetization angles from net effect of external field and anisotropy energy (Figure 4.13a(iii)). Whereas when two particles are in contact, dipolar effects cause magnetization to deviate from the direction of applied field (Figure 4.13 a(i)). Some spatial arrangements result in insignificant dipolar interactions depending on the overlap of field lines of two magnets. For example, two orthogonal particles in contact have least overlap in field lines if both their anisotropy axis are in the direction of applied field (Figure 4.13c(i)). Whereas if two particles are arranged parallelly, their field lines overlap such that dipole effects prevent

magnetization to align with field (Figure 4.13a(i)). Depending on the inter-particle distance and angle of arrangement, dipolar interactions cause magnetization to deviate more for some easy axis orientations[55] than the others as shown in Figure 4.13.

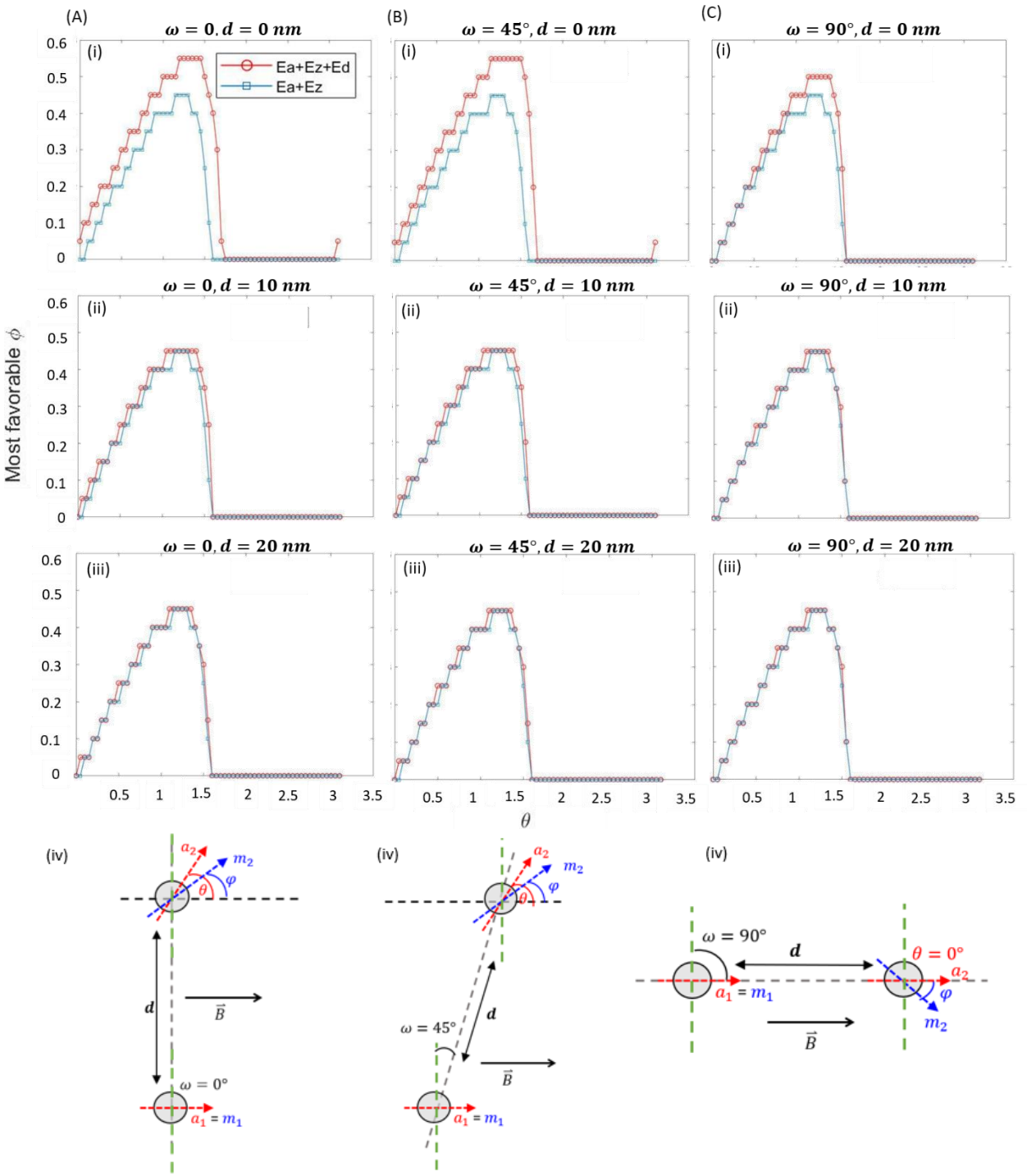

Figure 4.13: Panels (i)-(iii): Effect of dipole-dipole interactions between two particles on magnetization angles (ϕ) with respect to anisotropy axis (θ) for various inter-particle separations (d). x-axis is θ in radians and y-axis is ϕ in radians. (a) Two parallel particles, (b) two particles at 45°, (c) two orthogonal particles. Schematics for arrangements: (a), (b), (c) panel (iv).

(c) Demagnetizing Effects in Nanobowls

Similar results have been obtained experimentally and in simulations by several authors. Fu et.al. reported the dependence of anisotropy and magnetization on magnetic nanoparticle cluster size[99]. With simulations they showed that saturation magnetization decreased by 30% for clusters radius of 30nm as compared 5nm particles. This has been confirmed in other reports where clusters showed reduced magnetization and increased anisotropy[99,100]. For applicability to our data, it is important to note the net magnetic radius of nanobowls is 28nm and a ~50% reduction in magnetization from single IONPs is observed. Usov et.al. showed that cluster effects are significant for a packing density between 0.005 and 0.4. The cluster density at the surface of nanobowls is 0.31 and in the core is 0.009 indicating that is likely that IONP clusters are producing a demagnetizing effect on their nearest neighbors. These observations are tied together in the computational study by Klughertz et.al.[55]. They show that for close packed hexagonal 2D assemblies with random easy axis orientations, alignment with external field is harder due to long range order. The presence of defects gives rise to domains that contribute to demagnetizing effects. Point defects were created by removing particles in a homogenously distributed system giving rise to inter-particle distance larger or smaller than the mean. Domains have short range order and larger dipole fields than single particles. As a result, magnetization in nanoparticles deviates from applied field. This case is similar to what we see in our nanobowls wherein close-packed structures or domains are present on the surface. Therefore, the two-fold decrease in nanobowl M_s as compared to single IONPs can be attributed to contributions from demagnetizing effect of dipolar interactions.

4.4 Magnetic Drift Velocity (V_R) of Nanobowls

4.4.1 Guiding Efficiency, Particle Trajectory and V_R

In a NP suspension flowing in a microchannel, NPs are homogenously distributed along the channel diameter. In contrast, in small blood vessels, non-deformable NPs pushed toward the vessel wall as an effect of lift force, red blood cell (RBC) deformability and shear stress. As a result, NPs are distributed only at the periphery of the channel[48,101–104]. When a channel bifurcates, depending on its geometry, a portion of streamlines will flow in desired branch and the rest in the undesired branch (Figure 4.14a, b). It is assumed that NPs do not move across streamlines as their diffusion is negligible compared to advective velocities in most cases. Therefore, only NPs initially in streamlines flowing in the direction of desired branch will continue in that direction. However, all NPs in vessel must flow in desired direction in order to effectively minimize side-effects and reduce uptake by MPS organs. For this, NPs in streamlines going to undesired branch need to change trajectories so that they can flow to the desired direction instead.

We use external magnetic force to change particle trajectories of MNPs. Guiding efficiency is thus defined as the proportion of MNPs flowing into the desired branch. 100% guiding efficiency is achieved when all MNPs flow into the desired branch[21,44]. MNPs that are along streamlines flowing to desired branch, do not need external manipulation. For MNPs in all other streamlines, magnetic force is instrumental in initiating a trajectory change (Figure 4.14c). For the simplest case negligible gravitational settling forces and diffusion is assumed. In this case, when an MNP in convective flow is acted upon by magnetic force (F_M), it changes its velocity (speed and trajectory) to balance F_M and Stokes drag. Therefore, resultant particle trajectories are an important measure of guiding efficiency. If the resultant trajectory is in the desired direction, there is high guiding efficiency. Authors have developed frameworks to determine particle trajectories in the presence of different forces[47,72,73]. In our work, we only consider the influence of magnetic force and Stokes drag force. Stokes drag is defined by *in*

vivo fluid flow conditions specific to the application. F_M can be derived from SQUID measurements or from magnetic drift velocity (V_R) in a stagnant fluid.

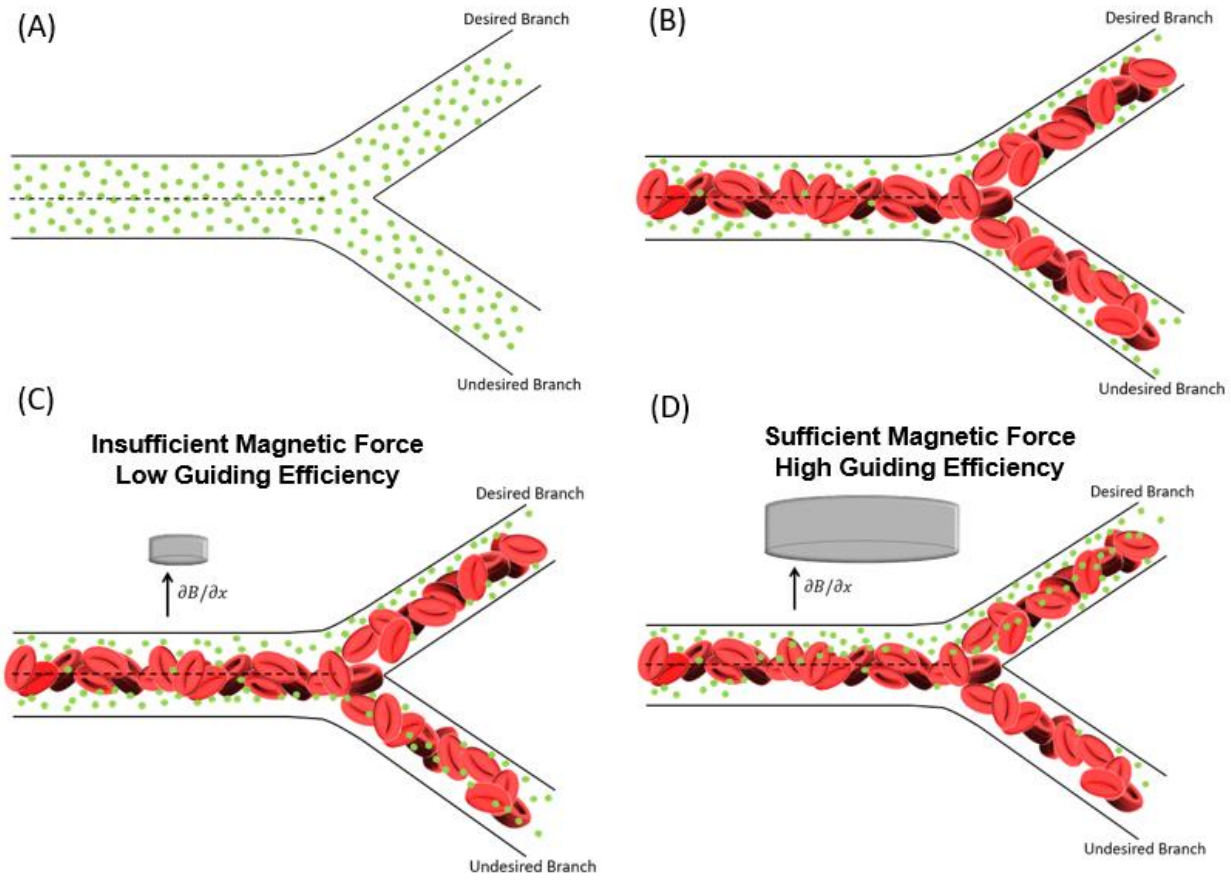

Figure 4.14: Microchannel with (a) suspension of only NPs. (b) suspension of RBCs and NPs. (c) Insufficient magnetic force giving low guiding efficiency. (d) Sufficient magnetic force giving high guiding efficiency

Magnetic drift velocity (V_R) is significant in guiding efficiency calculations as it provides a facile measurement to directly determine particle trajectories without explicit measurement of MNP moment. Resultant velocity ($\overrightarrow{V_P}$) can be solved from the vector sum of V_R and convective fluid velocity (V_L) for a given magnetic field gradient ($\nabla\vec{B}$) (equation 2.33). MNP's response to a $\nabla\vec{B}$ is resolved into resultant speed and the resultant angle. The direction of branch is also represented as an angle. In a straight channel, the geometric system is defined such that the resultant angle and desired angle of guiding are with respect to direction of fluid flow. If

$|\boldsymbol{V_P}|>|\boldsymbol{V_L}|$**,** and the resultant angle is in the desired direction, MNP is efficiently guided. Previously, authors have used imaging to determine V_R of microparticles and magnetosomes[50,105,106]. Here, we measure concentration flux in a magnetic field gradient to determine V_R in the *accumulation assay.*

4.4.2 Accumulation assay for measuring flux in $\nabla\vec{B}$

In the accumulation assay, rate of change of concentration ($\partial c/\partial t$) due to magnetic field gradient was measured to determine V_R of MNPs Size exclusion was performed to isolate particles size less than 0.45um. Commercially bought 15nm IONP and 60nm IONP were used as controls to characterize the assay. 15nm Iron oxide is characterized in section 4.1.3 and 4.3. 60nm iron oxide are $56 \pm 16nm$ in diameter from SEM images with a hydrodynamic diameter of ~65nm, and have a M_s of ~20emu/g. As expected, the concentration at the location closest to magnet increases with time, and concentration at the location furthest from the magnet decreases with time (Figure 4.15a). Concentrations in the center of the well show fluctuating behavior with time (Figure 4.15b). $\partial c/\partial t$ without a magnet (Figure 4.15c) is an order of magnitude smaller than that with a magnet (Figure 4.15d). Fluctuations in concentration without magnet can be considered to be noise due to diffusion and gravitational settling for heavier particles.

4.4.3 Accumulation assay Characterization

Magnetic drift velocities derived from this assay are shown in Figure 4.15d. A student's t-test gives p-values < 0.01 for comparison of all three velocities indicating that the assay can distinguish between increments as small as 0.09um/s with current parameters. Standard deviations for commercial particles were 25-30% indicating reasonable repeatability.

Studies have used optical measurements of V_R as a facile method to determine magnetic moment of samples that cannot be kept in vacuum, like magnetosomes[50,105,106]. Here we compare V_R derived from SQUID magnetization measurements and size characterization

(Equation 2.30) to those directly measured from the accumulation assay. For control samples, there is 16% discrepancy between SQUID and assay values. There is 28% variability in measurements of the same batch. To evaluate the batch-to-batch variability in nanobowls, two batches were tested on SQUID and three with this assay. The variability from SQUID measurements was 28%, close to the variability in IO content – 30% from image analysis. However, this assay shows a variability of 34%. In conclusion, this assay can be used as a facile measurement of magnetic moment and V_R albeit with compromised precision and accuracy. Several parameters can be used to increase the sensitivity of the assay like chamber geometry, magnet strength and fluorescent labeling in case of dilute samples. The magnetic field gradient can be chosen to be application specific. In this study, we chose high magnetic field gradient of 26.9T/m compared to those available on MRI machines (4-15 T/m on average, maximum of 100T/m[107]).

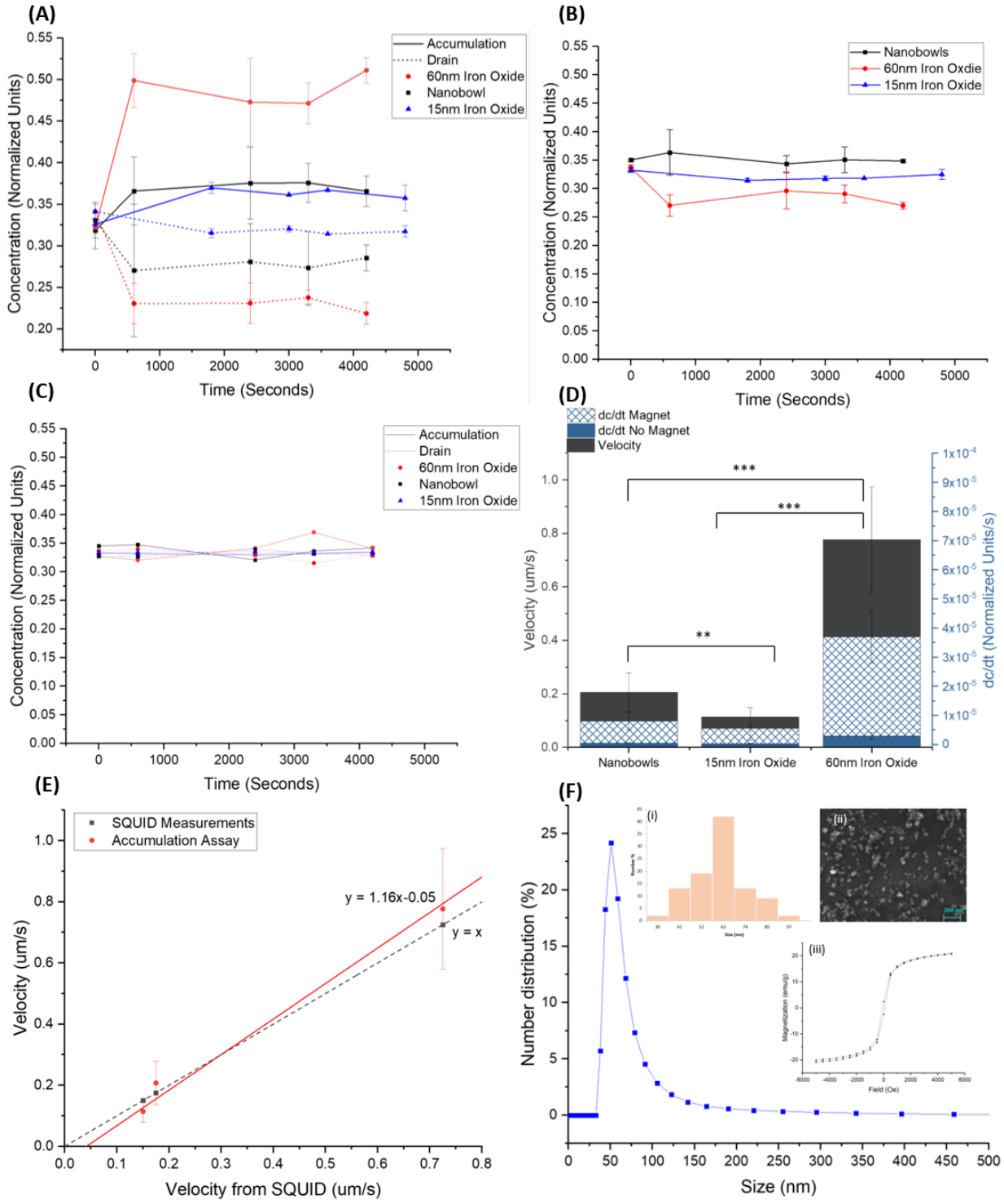

*Figure 4.15: Concentration as a function of time at (a) accumulation and drain sites for attraction toward magnet (b) center of well (c) accumulation and drain sites without magnet. (d) Velocity and $\partial c/\partial t$ for three samples with and without magnet. (*** = p<0.005, ** = p<0.01). (e) Experimental velocity from accumulation assay (Eqn 3.1) as compared to that derived from SQUID measurements (Eqn 2.30). (f) 60nm iron oxide DLS size distribution, inset (i) size histogram from SEM images, (ii) SEM image (iii) Mvs H.*

4.4.4 Predicting Single Nanobowl Trajectories

A simple workflow is suggested to determine guiding efficiency from V_R as outlined below. The following sections walk through the steps of this workflow and validating its calculations.

Workflow for determining Guiding Efficiency from $\overrightarrow{V_R}$:

(1) Measure $\overrightarrow{V_R}$ using the accumulation assay

(2) Determine the geometry and flow characteristics of the bifurcation in targeting region

(3) Choosing a magnetic field gradient for the application

(4) Determine vector sum of $\overrightarrow{V_R}$ and fluid velocity in targeting region

(5) Compare resultant angle to angle of targeting bifurcation

Resultant particle trajectories can be found from Equation 2.33 that is derived from the balance of magnetic and Stokes drag forces: $\overrightarrow{\boldsymbol{V_p}} = \overrightarrow{\boldsymbol{V_R}} + \overrightarrow{\boldsymbol{V_l}}$. In this section we show predictive calculations for nanobowl response ($\overrightarrow{\boldsymbol{V_p}}$) in different conditions. $\overrightarrow{\boldsymbol{V_p}}$ is resolved into resultant speed and angle.

Case 1: *in vitro* imaging performed in this study

Parameters:

(a) Magnetic field gradient: 0.269T/cm applied perpendicular to fluid flow

(b) 0.2μm/s $\left|\overrightarrow{V_R}\right|$ as measured from accumulation assay

(c) Fluid velocity: 15μm/s

Results:

(a) Resultant speed: 15 μm/s

(b) Resultant angle: 0.76°

Case 2: Minimum healthy physiological velocity

Parameters:

(a) Magnetic field gradient: 0.269T/cm applied perpendicular to fluid flow

(b) 0.2μm/s $\left|\overrightarrow{V_R}\right|$ as measured from accumulation assay

(c) Fluid velocity: 1 mm/s

Results:

(a) Resultant speed: 1mm/s

(b) Resultant angle: 0.01°

4.4.5 Modeling Nanobowl Cluster Magnetic Drift Velocity

An attempt was a made to calculate for nanobowl cluster magnetic drift velocity. To confirm calculations, clusters were imaged on a microscope to measure magnetic drift velocity. Measurements of V_R were made by acquiring time lapse videos of particles under magnetic gradient. Clusters were estimated as spheres with diameter equivalent to their longest axis (measured from images). To calculate magnetic and drag force on clusters, a scale up approach was used:

(a) No. of nanobowls per cluster (n) = $\frac{cluster\ diameter}{avg.SEM\ diamter\ per\ nanobowl}$

(b) Radius of nanobowl clusters (r_c) = $avg.SEM\ radius\ per\ nanobowl\ x\ n$

(c) IONPs per cluster = $average\ IONP\ per\ nanobowl\ x\ no.of\ bowls\ per\ cluster$

(d) Magnetic radius ($r_{m,c}$) = volume equivalent spherical radius of all IONPs in cluster

(e) Magnetic force $\boldsymbol{F_{m,c}}$ =

$M\left(magnetization\ from\ SQUID, \frac{emu}{g}\right) x\ \frac{4}{3}\pi {r_{m,c}}^3\ x\ density\ of\ IO\ \left(5\frac{mg}{ml}\right) x\mu_o$

(f) $\boldsymbol{V_R} = \frac{\boldsymbol{F_{m,c}}}{6\pi r_c \eta}$

Magnetic force on nanobowl clusters increases as cluster size increases (Figure 4.16b) due to a proportional increase in IO volume. Drag force acting on clusters also increases with cluster size and V_R depends on the ratio $\frac{magnetic\ radius^3}{cluster\ radius}$.

Validating nanocluster $\boldsymbol{V_R}$ calculations from Imaging

V_R increases with an increase in cluster size as magnetic radius has a greater influence on it (Figure 4.16a). Figure 4.16a shows a comparison of calculated and imaged values for different cluster sizes. There is good agreement for small cluster sizes for SQUID measurements made in aqueous solutions. It is important to note that SQUID measurements of

nanobowl powders gave gross underestimates (data not shown). At larger sizes, experimental values are either over-estimated or under-estimated. This could be due to biased size measurements as larger clusters move out of the plane of focus as they travel. Another possibility is the approximation of clusters as spheres. In reality, there is no way two-three nanoparticles could cluster in a spherical shape. This analysis shows that using the scale up approach we can determine nanobowl cluster magnetic behavior with at most 14% variability. It follows that single particle magnetic behavior may be estimated from clusters with the same margin of error.

4.4.6 Predicting Nanobowl Cluster Trajectories

Case 1: 3 Nanobowl cluster

Parameters:

(a) Magnetic field gradient: 0.269T/cm applied perpendicular to fluid flow

(b) 0.627μm/s $\left|\overrightarrow{V_R}\right|$ as measured from accumulation assay

(c) Fluid velocity: 10 μm/s

Results:

(a) Resultant speed: 10.0 μm/s

(b) Resultant angle: 3.43°

Case 1: 2 Nanobowl cluster

Parameters:

(a) Magnetic field gradient: 0.269T/cm applied perpendicular to fluid flow

(b) 0.278μm/s $\left|\overrightarrow{V_R}\right|$ as measured from accumulation assay

(c) Fluid velocity: 15 μm/s

Results:

(a) Resultant speed: 15.0 μm/s

(b) Resultant angle: 1.06°

4.4.7 Validating Predicted Nanobowl Cluster Trajectories

Here we image nanobowls in different forces to understand their behavior. The imaging technique used was brightfield imaging in high magnification. Although fluorescence imaging

gives greater size resolution, the long exposure times make it hard to follow particle trajectories. Therefore, brightfield imaging was used with the tradeoff being that only particles larger than 300nm could be imaged. Figure 4.17 shows nanobowl cluster trajectories in different conditions. In the absence of magnetic force, clusters show random trajectories in suspension due to collisions with surrounding molecules and other particles (Figure 4.17a). When a magnetic force is applied on them, they move in the direction of the force (Figure 4.17b). In convective flow, clusters travels along fluid trajectories (Figure 4.17c). Larger clusters travel at slower velocities due to larger drag and inertial forces; measured velocities are in the range 10-15μm/s. Upon the application of a magnetic field gradient in fluid flow, nanobowls show small deviations (resultant angle) in the direction of applied gradient. Smaller clusters (≤ 2 nanobowls) cannot continue along that trajectory as drag force exceeds magnetic force, consequently, the cluster follows fluid flow (Figure 4.17b). An increase in magnetic force corresponded with an increase in V_R and initial deviation angle (resultant angle). However, resultant velocities did not change significantly as magnetic force acting on particles was an order of magnitude smaller than drag force. It was observed that larger clusters (>2.5 nanobolws per cluster) were able to maintain trajectories along initial deviations for larger distance attributed to greater magnetic forces. Imaged resultant angles for smaller clusters are in close agreement with those from calculations. Whereas, for larger clusters (≥ 3 nanobowls) resultant angles are upto three times larger than those calculated.

These results are in agreement with previous experimental and computational studies where particle trajectories for sizes ranging from 50nm to 1um and magnetic field gradients 7 T/m to 200 T/m in convection velocities of 1mm/s – 10cm/s[46,72,108] have been determined. They have shown that particles experiencing a magnetic force stronger than drag force change trajectories more drastically (with larger resultant angles) and are able to continue along that trajectory. In contrast, particles experiencing magnetic forces weaker than drag force make less

prominent deviations in trajectory toward magnetic force and are unable to continue along that trajectory. In this study, for the largest cluster imaged, $F_M = 10^{-14}N$ and $F_D = 10^{-13}N$, therefore resulting in the latter of the two behaviors verifying that the response of a magnetic particle depends on the ratio of magnetic and drag forces.

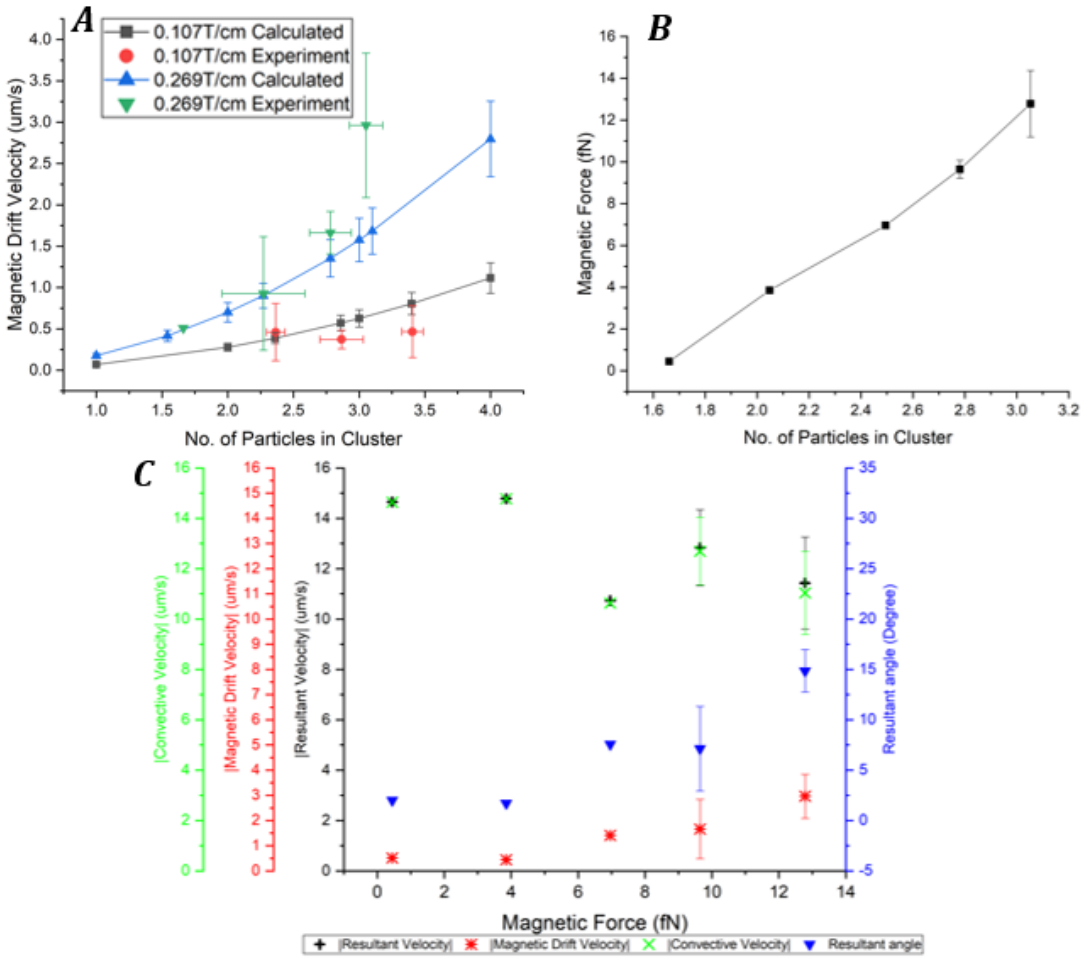

Figure 4.16: (a) Magnetic drift velocity as a function of no. of particles in cluster. Calculated from scale up equations and measured from time lapse imaging. (b) Scaling of magnetic force with particle cluster size. (c) Magnetic, convective, resultant velocity and resultant trajectory angle as it varies with magnetic force.

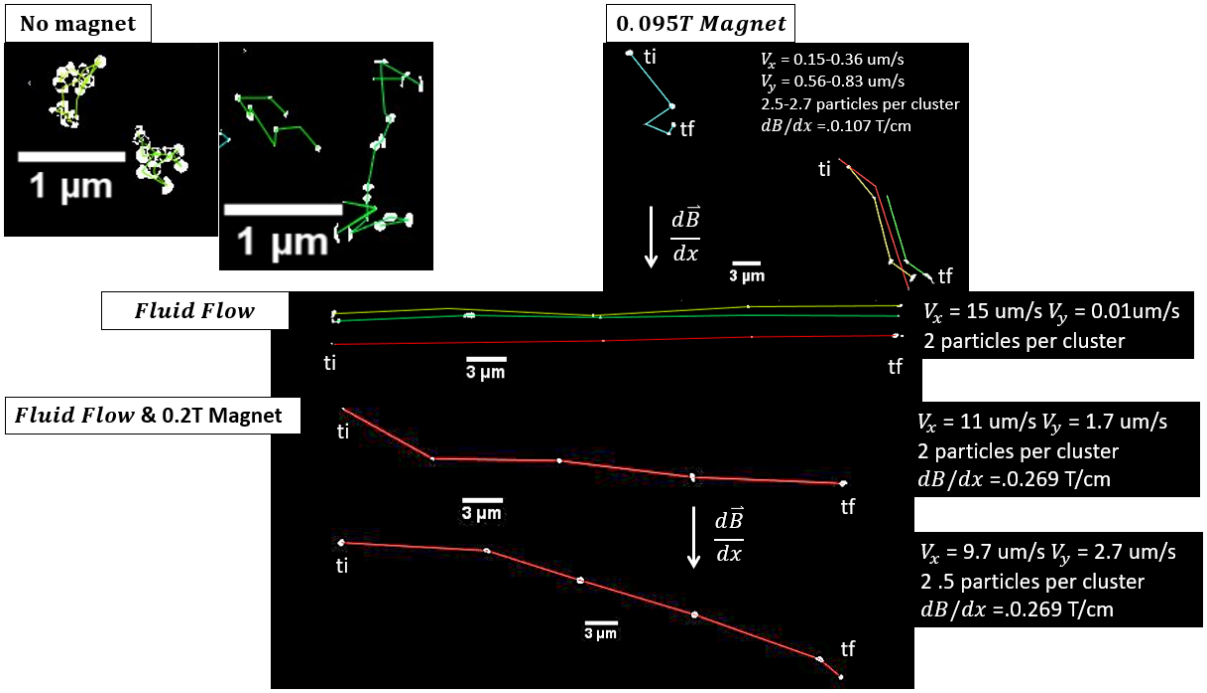

Figure 4.17: Example trajectories of nanobowl clusters in different conditions. ti = initial position, tf=final position after 5 or more frames. Arrow points in the direction of magnetic field gradient.

4.4.8 Applications of mathematical framework in physiological conditions

We show that a simple scale-up approach can predict nanobowl cluster magnetic drift velocities ($\boldsymbol{V_R}$). We are also able to show that $\boldsymbol{V_R}$ is successfully able to predict resultant trajectories for small nanobowl clusters. As it follows from these observations, we attempt to use $\boldsymbol{V_R}$ measured from the accumulation assay to predict single nanobowl behavior in the aortic arch bifurcation to determine guiding efficiency to the brain. In the future, single nanobowl trajectories can be confirmed by dark field microcopy, a high resolution imaging technique, that has been shown to image with high spatial resolution upto 20nm[109,110].

Case: Aortic Arch bifurcation (Figure 4.18)

Parameters:

(a) Magnetic field gradient: 0.269T/cm applied 80° to fluid flow

(b) 0.2µm/s $\left|\overrightarrow{V_R}\right|$ as measured from accumulation assay

(c) Fluid velocity: 60-75cm/s[111,112]

(d) Desired resultant angle: ~54° in a type II arch[113]

Results:

(a) Resultant speed: 60cm/s

(b) Resultant angle: ~$10^{-5\circ}$

Using the same approach, we determine that for guiding particles in this geometry and convection velocity, the minimum magnetic drift velocity should be ~62cm/s and the field gradient direction ~113° to induce any noticeable effects. Given that the magnetic field gradient used in this study was one of the highest available, this analysis illuminates that the ratio of magnetic force and drag force on nanobowls, does not yield desired deviations (as much as 54°) for guiding particles to the brain at the aortic arch bifurcation. This calls for magnetic materials with magnetic moments, and by extension magnetic drift velocities, that are comparable to physiological drag forces at practically achievable magnetic field gradients.

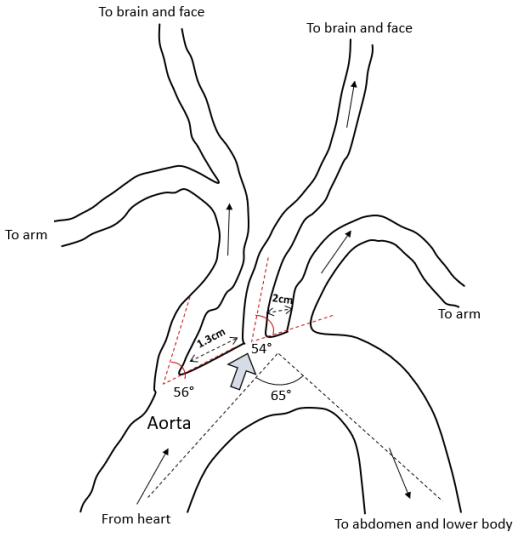

Figure 4.18 Type II Aortic arch geometry with parameters from Demertzis et.al.[113]*. Grey arrow shows branch of interest for delivery to brain.*

Chapter 5

Conclusion

5.1 Summary of Work

This thesis details the design and efficiency of nanobowls for applications in targeted drug delivery to the brain. The overarching goal of designing this technology is to use external magnetic field gradients to guide payload carrying nanobowls to the brain through blood vessel networks, thus avoiding sequestering by phagocytic organs. A facile workflow of calculations and *in vitro* measurements is constructed for predicting guiding efficiency.

Nanobowls are composite magnetic nanoparticles (MNPs) or Iron oxide (IO) and silica. Their important features are:

(1) Average hydrodynamic diameter of 280nm and zeta potential of 23mV, conferring them intermittent stability of upto 3 days upon storage in 4°C.

(2) Average saturation magnetization of 40 emu/g, average magnetic volume per nanobowl of $10^{-22}m^3$ and Large magnetic moment of $2x10^{-17}Am^2$.

(3) Potentially enhanced biocompatibility by (a) preventing iron oxide exposure by silica coating, (b) PEG-silane modification on outer most layer.

(4) Bowl- like pit for drug loading post processing.

Balance of magnetic force and Stokes drag force allows for the derivation of a simple expression for resultant nanobowl trajectory. This expression consists of the vector sum of magnetic drift velocity ($\overrightarrow{V_R}$) and fluid flow velocity. To this end, an assay has been designed and characterized for facile measurement of $\overrightarrow{V_R}$ without cumbersome high-resolution imaging or SQUID measurements. The assay works by measuring concentration flux in a magnetic field gradient. It shows 16% difference from SQUID measurements and similar repeatability. It is further validated that for small nanobowl clusters, calculations based on $\overrightarrow{V_R}$ measurements serve

as a good predictor of their trajectories. Therefore, a simple workflow for determining guiding efficiency can be outlined as:

(1) Measuring $\overrightarrow{V_R}$ using the accumulation assay

(2) Determining the geometry and flow characteristics of the bifurcation in targeting region

(3) Choosing a magnetic field gradient for the application

(4) Determining vector sum of $\overrightarrow{V_R}$ and fluid velocity in targeting region

(5) Comparing resultant angle to angle of targeting bifurcation

Upon application of this workflow to physiological conditions it is found that a $\overrightarrow{V_R}$ several orders or magnitude larger than that of nanobowls is needed for efficient guiding in the aortic arch bifurcation.

5.2 Future Work

It is important to note that the *in vitro* work described here involves suspensions of solely, nanobowls. However, it has been shown that the effect of red blood cells (RBC) on the fluidics and trajectories of MNPs is not trivial. It is possible that a larger magnetic force is required to overcome RBC-MNP interactions than predicted by the framework here. Therefore, a more comprehensive predictive model is required that takes into consideration dynamics of physiological blood flow.

The next steps toward the fulfilment of this technology would come in two main areas: (1) development of large magnetic drift velocity nanocarriers and (2) designing localized field gradients specific to the geometry of the aortic arch bifurcation. Additional aspects that need further investigation are:

(1) Stability of these carriers in biological media

(2) Overall biocompatibility – including tests for histo-, cyto-, hemo- and immuno-compatibility

(3) Ability of these carriers to penetrate the blood brain barrier

(4) Drug release and toxicity kinetics

BIBLIOGRAPHY

1. Parnell, E., Smith, B. O., Palmer, T. M., Terrin, A., Zaccolo, M. & Yarwood, S. J. Regulation of the inflammatory response of vascular endothelial cells by EPAC1. *Br. J. Pharmacol.* **166**, 434–46 (2012).

2. Torchilin, V. P. Passive and Active Drug Targeting: Drug Delivery to Tumors as an Example. in *Handbook of experimental pharmacology* 3–53 (2010). doi:10.1007/978-3-642-00477-3_1

3. Singh, R., Lillard, J. W. & Jr. Nanoparticle-based targeted drug delivery. *Exp. Mol. Pathol.* **86**, 215–23 (2009).

4. Hayashi, K., Nakamura, M., Miki, H., Ozaki, S., Abe, M., Matsumoto, T., Sakamoto, W., Yogo, T. & Ishimura, K. Magnetically responsive smart nanoparticles for cancer treatment with a combination of magnetic hyperthermia and remote-control drug release. *Theranostics* **4**, 834–44 (2014).

5. Hua, X., Yang, Q., Dong, Z., Zhang, J., Zhang, W., Wang, Q., Tan, S. & Smyth, H. D. C. Magnetically triggered drug release from nanoparticles and its applications in anti-tumor treatment. *Drug Deliv.* **24**, 511–518 (2017).

6. Kong, S. D., Zhang, W., Lee, J. H., Brammer, K., Lal, R., Karin, M. & Jin, S. Magnetically Vectored Nanocapsules for Tumor Penetration and Remotely Switchable On-Demand Drug Release. *Nano Lett.* **10**, 5088–5092 (2010).

7. Zhao, P., Zheng, M., Luo, Z., Gong, P., Gao, G., Sheng, Z., Zheng, C., Ma, Y. & Cai, L. NIR-driven Smart Theranostic Nanomedicine for On-demand Drug Release and Synergistic Antitumour Therapy. *Sci. Rep.* **5**, 14258 (2015).

8. Xiong, F., Nirupama, S., Sirsi, S. R., Lacko, A. & Hoyt, K. Ultrasound-Stimulated Drug Delivery Using Therapeutic Reconstituted High-Density Lipoprotein Nanoparticles. *Nanotheranostics* **1**, 440–449 (2017).

9. Varma, V. N. S. K., Shivakumar, H. G., Balamuralidhara, V., Navya, M. & Hani, U. Development of pH Sensitive Nanoparticles for Intestinal Drug Delivery Using Chemically Modified Guar Gum Co-Polymer. *Iran. J. Pharm. Res. IJPR* **15**, 83–94 (2016).

10. Liu, L., Yao, W., Rao, Y., Lu, X. & Gao, J. pH-Responsive carriers for oral drug delivery: challenges and opportunities of current platforms. *Drug Deliv.* **24**, 569–581 (2017).

11. Wang, L., Jang, G., Ban, D. K., Sant, V., Seth, J., Kazmi, S., Patel, N., Yang, Q., Lee, J., Janetanakit, W., Wang, S., Head, B. P., Glinsky, G. & Lal, R. Multifunctional stimuli responsive polymer-gated iron and gold-embedded silica nano golf balls: Nanoshuttles for targeted on-demand theranostics. *Bone Res.* **5**, 1–14 (2017).

12. Li, W., Cai, X., Kim, C., Sun, G., Zhang, Y., Deng, R., Yang, M., Chen, J., Achilefu, S., Wang, L. V & Xia, Y. Gold nanocages covered with thermally-responsive polymers for controlled release by high-intensity focused ultrasound. *Nanoscale* **3**, 1724–30 (2011).

13. Yu, B., Tai, H. C., Xue, W., Lee, L. J. & Lee, R. J. Receptor-targeted nanocarriers for therapeutic delivery to cancer. *Mol. Membr. Biol.* **27**, 286–98 (2010).

14. Zhong, Y., Meng, F., Deng, C. & Zhong, Z. Ligand-Directed Active Tumor-Targeting Polymeric Nanoparticles for Cancer Chemotherapy. *Biomacromolecules* **15**, 1955–1969 (2014).

15. Kou, L., Sun, J., Zhai, Y. & He, Z. The endocytosis and intracellular fate of nanomedicines: Implication for rational design. *Asian J. Pharm. Sci.* **8**, 1–10 (2013).

16. Giustini, A. J., Petryk, A. A., Cassim, S. M., Tate, J. A., Baker, I. & Hoopes, P. J. MAGNETIC NANOPARTICLE HYPERTHERMIA IN CANCER TREATMENT. *Nano Life* **1**, (2010).

17. Chatterjee, D. K., Diagaradjane, P. & Krishnan, S. Nanoparticle-mediated hyperthermia in cancer therapy. *Ther. Deliv.* **2**, 1001–14 (2011).

18. Zhou, Y., Peng, Z., Seven, E. S. & Leblanc, R. M. Crossing the blood-brain barrier with nanoparticles. *J. Control. Release* **270**, 290–303 (2018).

19. Gidwani, M. & Singh, A. V. Nanoparticle enabled drug delivery across the blood brain barrier: in vivo and in vitro models, opportunities and challenges. *Curr. Pharm. Biotechnol.* **14**, 1201–12 (2014).

20. Patel, M. M. & Patel, B. M. Crossing the Blood–Brain Barrier: Recent Advances in Drug Delivery to the Brain. *CNS Drugs* **31**, 109–133 (2017).

21. Hoshiar, A., Le, T.-A., Amin, F., Zhang, X., Kim, M. & Yoon, J. *Noninvasive Guidance Scheme Delivery in Alzheimer ' s Disease*. (CRC Press, 2018).

22. Pandey, P. K., Sharma, A. K. & Gupta, U. Blood brain barrier: An overview on strategies in drug delivery, realistic in vitro modeling and in vivo live tracking. *Tissue barriers* **4**, e1129476 (2016).

23. Saraiva, C., Praça, C., Ferreira, R., Santos, T., Ferreira, L. & Bernardino, L. Nanoparticle-mediated brain drug delivery: Overcoming blood-brain barrier to treat neurodegenerative diseases. *J. Control. Release* **235**, 34–47 (2016).

24. Yamazaki, Y. & Kanekiyo, T. Blood-Brain Barrier Dysfunction and the Pathogenesis of Alzheimer's Disease. *Int. J. Mol. Sci.* **18**, (2017).

25. Alyautdin, R. N., Petrov, V. E., Langer, K., Berthold, A., Kharkevich, D. A. & Kreuter, J. Delivery of Loperamide Across the Blood-Brain Barrier with Polysorbate 80-Coated Polybutylcyanoacrylate Nanoparticles. *Pharm. Res.* **14**, 325–328 (1997).

26. Voigt, N., Henrich-Noack, P., Kockentiedt, S., Hintz, W., Tomas, J. & Sabel, B. A. Surfactants, not size or zeta-potential influence blood–brain barrier passage of polymeric nanoparticles. *Eur. J. Pharm. Biopharm.* **87**, 19–29 (2014).

27. Lockman, P. R., Mumper, R. J., Khan, M. A. & Allen, D. D. Nanoparticle Technology for Drug Delivery Across the Blood-Brain Barrier. *Drug Dev. Ind. Pharm.* **28**, 1–13 (2002).

28. Chertok, B., Moffat, B. A., David, A. E., Yu, F., Bergemann, C., Ross, B. D. & Yang, V. C. Iron oxide nanoparticles as a drug delivery vehicle for MRI monitored magnetic targeting of brain tumors. *Biomaterials* **29**, 487–496 (2008).

29. Hammarlund-Udenaes, M., Fridén, M., Syvänen, S. & Gupta, A. On the rate and extent of drug delivery to the brain. *Pharm. Res.* **25**, 1737–50 (2008).

30. Gustafson, H. H., Holt-Casper, D., Grainger, D. W. & Ghandehari, H. Nanoparticle Uptake: The Phagocyte Problem. *Nano Today* **10**, 487–510 (2015).

31. Blanco, E., Shen, H. & Ferrari, M. Principles of nanoparticle design for overcoming biological barriers to drug delivery. *Nat. Biotechnol.* **33**, 941–51 (2015).

32. Busquets, M. A., Espargaró, A., Sabaté, R. & Estelrich, J. Magnetic Nanoparticles Cross the Blood-Brain Barrier: When Physics Rises to a Challenge. *Nanomater. (Basel, Switzerland)* **5**, 2231–2248 (2015).

33. D'Agata, F., Ruffinatti, F. A., Boschi, S., Stura, I., Rainero, I., Abollino, O., Cavalli, R. & Guiot, C. Magnetic nanoparticles in the central nervous system: Targeting principles, applications and safety issues. *Molecules* **23**, 1–25 (2018).

34. Chomoucka, J., Drbohlavova, J., Huska, D., Adam, V., Kizek, R. & Hubalek, J. Magnetic nanoparticles and targeted drug delivering. *Pharmacol. Res.* **62**, 144–149 (2010).

35. Raut, S. L., Kirthivasan, B., Bommana, M. M., Squillante, E. & Sadoqi, M. The formulation, characterization and *in vivo* evaluation of a magnetic carrier for brain delivery of NIR dye. *Nanotechnology* **21**, 395102 (2010).

36. Kong, S. D., Zhang, W., Lee, J. H., Brammer, K., Lal, R., Karin, M. & Jin, S. Magnetically Vectored Nanocapsules for Tumor Penetration and Remotely Switchable On-Demand Drug Release. (2010). doi:10.1021/nl1033733

37. Kong, S. D., Lee, J., Ramachandran, S., Eliceiri, B. P., Shubayev, V. I., Lal, R. & Jin, S. Magnetic targeting of nanoparticles across the intact blood-brain barrier. *J. Control. Release* **164**, 49–57 (2012).

38. Lee, K., David, A. E., Zhang, J., Shin, M. C. & Yang, V. C. Enhanced accumulation of theranostic nanoparticles in brain tumor by external magnetic field mediated in situ clustering of magnetic nanoparticles. *J. Ind. Eng. Chem.* **54**, 389–397 (2017).

39. Shapiro, B., Kulkarni, S., Nacev, A., Muro, S., Stepanov, P. Y. & Weinberg, I. N. Open challenges in magnetic drug targeting. *Wiley Interdiscip. Rev. Nanomed. Nanobiotechnol.* **7**, 446–57 (2015).

40. Shapiro, B. Towards dynamic control of magnetic fields to focus magnetic carriers to targets deep inside the body. *J. Magn. Magn. Mater.* **321**, 1594–1599 (2009).

41. Sarwar, A., Nemirovski, A. & Shapiro, B. Optimal Halbach permanent magnet designs for maximally pulling and pushing nanoparticles. *J. Magn. Magn. Mater.* **324**, 742–754 (2012).

42. Shapiro, B., Dormer, K. & Rutel, I. B. A two-magnet system to push therapeutic nanoparticles. *AIP Conf. Proc.* **1311**, 77–88 (2010).

43. Bente, K., Codutti, A., Bachmann, F. & Faivre, D. Biohybrid and Bioinspired Magnetic Microswimmers. *Small* **1704374**, 1–25 (2018).

44. Grief, A. D. & Richardson, G. Mathematical modelling of magnetically targeted drug delivery. *J. Magn. Magn. Mater.* **293**, 455–463 (2005).

45. *Clinical Applications of Magnetic Nanoparticles*. (CRC Oress, 2018).

46. Sharma, S., Katiyar, V. K. & Singh, U. Mathematical modelling for trajectories of magnetic nanoparticles in a blood vessel under magnetic field. *J. Magn. Magn. Mater.* **379**, 102–107 (2015).

47. Cherry, E. M., Maxim, P. G. & Eaton, J. K. Particle size, magnetic field, and blood velocity effects on particle retention in magnetic drug targeting; Particle size, magnetic field, and blood velocity effects on particle retention in magnetic drug targeting. (2009).

doi:10.1118/1.3271344.

48. Ye, H., Shen, Z. & Li, Y. Computational modeling of magnetic particle margination within blood flow through LAMMPS. *Comput. Mech.* 1–20 (2017). doi:10.1007/s00466-017-1508-y

49. Manuscript, A. & Structures, T. The Behaviors of Ferro-Magnetic Nano-Particles In and Around Blood Vessels under Applied Magnetic Fields. **6**, 247–253 (2009).

50. Heidsieck, A., Vosen, S., Zimmermann, K., Wenzel, D. & Gleich, B. Analysis of trajectories for targeting of magnetic nanoparticles in blood vessels. *Mol. Pharm.* **9**, 2029–2038 (2012).

51. Heidsieck, A., Rudigkeit, S., Rümenapp, C. & Gleich, B. Simple optical measurement of the magnetic moment of magnetically labeled objects. (2017). doi:10.1016/j.jmmm.2016.10.057

52. Thomsen, L. B., Thomsen, M. S. & Moos, T. Targeted drug delivery to the brain using magnetic nanoparticles. *Ther. Deliv.* **6**, 1145–1155 (2015).

53. Mannell, H., Pircher, J., Räthel, T., Schilberg, K., Zimmermann, K., Pfeifer, A., Mykhaylyk, O., Gleich, B., Pohl, U. & Krötz, F. Targeted Endothelial Gene Delivery by Ultrasonic Destruction of Magnetic Microbubbles Carrying Lentiviral Vectors. *Pharm. Res.* **29**, 1282–1294 (2012).

54. Sánchez, F. H., Mendoza Zélis, P., Arciniegas, M. L., Pasquevich, G. A. & Fernández van Raap, M. B. Dipolar interaction and demagnetizing effects in magnetic nanoparticle dispersions: Introducing the mean-field interacting superparamagnet model. *Phys. Rev. B* **95**, 134421 (2017).

55. Klughertz, G., Manfredi, G., Hervieux, P.-A., Pichon, B. P. & Begin-Colin, S. Effect of Disorder and Dipolar Interactions in Two-Dimensional Assemblies of Iron-Oxide Magnetic Nanoparticles. *J. Phys. Chem. C* **120**, 7381–7387 (2016).

56. Brinis, D., Laggoun, A., Ledue, D. & Patte, R. Effects of dimensionality and spatial distribution on the magnetic relaxation of interacting ferromagnetic nanoclusters: A Monte Carlo study. *J. Appl. Phys. J. Appl. Phys. J. Appl. Phys. Superparamagnetism J. Appl. Phys.* **115**, 173906–123909 (2014).

57. Kuch, W. *Magnetic Imaging*.

58. Hiemenz, P. C. *Principles of Colloid and Surface Chemistry*. (Marcel Dekker, 1986).

59. Ortega, D. Structure and magnetism in magnetic nanoparticles. *Magn. nanoparticles from Fabr. to Biomed. Clin. Appl.* 3–44 (2011).

60. Akpinar, B., Fielding, L. A., Cunningham, V. J., Ning, Y., Mykhaylyk, O. O., Fowler, P. W. & Armes, S. P. Determining the Effective Density and Stabilizer Layer Thickness of Sterically Stabilized Nanoparticles. *Macromolecules* **49**, 5160–5171 (2016).

61. Higashitani, K., Nakamura, K., Shimamura, T., Fukasawa, T., Tsuchiya, K. & Mori, Y. Orders of Magnitude Reduction of Rapid Coagulation Rate with Decreasing Size of Silica Nanoparticles. *Langmuir* **33**, 5046–5051 (2017).

62. Nalwa, H. S. *Handbook of Surfaces and Interfaces of Materials: zeolites*. *Handbook of Surfaces and Interfaces of Materials* **2**, (2001).

63. Mccartney, L. N. & Levine, A. S. An Improvement for the Double on Deriaguin's Expression Layer Interaction Energy Colloidal Particles at Small Potentials of Two Spherical.

64. Kim, S. Y. & Zukoski, C. F. Particle restabilization in silica/PEG/ethanol suspensions: How strongly do polymers need to adsorb to stabilize against aggregation? *Langmuir* **27**, 5211–5221 (2011).

65. Zęibacz, N., Wieczorek, S. A., Kalwarczyk, T., Fiałkowski, M. & Hołyst, R. Crossover regime for the diffusion of nanoparticles in polyethylene glycol solutions: Influence of the depletion layer. *Soft Matter* **7**, 7181–7186 (2011).

66. Ku, J. G., Liu, X. Y., Chen, H. H., Deng, R. D. & Yan, Q. X. Interaction between two magnetic dipoles in a uniform magnetic field. *AIP Adv.* **6**, 25004–25005 (2016).

67. Jeong, U., Teng, X., Wang, Y., Yang, H. & Xia, Y. Superparamagnetic Colloids: Controlled Synthesis and Niche Applications. *Adv. Mater.* **19**, 33–60 (2007).

68. Arruebo, M., Fernández-Pacheco, R., Ibarra, M. R. & Santamaría, J. Magnetic nanoparticles for drug delivery. *Nano Today* **2**, 22–32 (2007).

69. Coey, J. M. . *Magnetism and Magnetic Materials*. (Cambridge University Press, 2010).

70. Kolhatkar, A. G., Jamison, A. C., Litvinov, D., Willson, R. C. & Lee, T. R. *Tuning the magnetic properties of nanoparticles*. *International Journal of Molecular Sciences* **14**, (2013).

71. Lalena, J. & Cleary, D. *Principles of Inorganic Materials Design*. (John Wiley & Sons, 2005).

72. Sinha, A., Ganguly, R., De, A. K. & Puri, I. K. Single magnetic particle dynamics in a microchannel. doi:10.1063/1.2780191

73. Haverkort, J. W., Kenjereš, S., Kleijn, C. R. & Burgers, J. M. Magnetic particle motion in a Poiseuille flow. doi:10.1103/PhysRevE.80.016302

74. Mo, A. H., Landon, P. B., Emerson, C. D., Zhang, C., Anzenberg, P., Akkiraju, S. & Lal, R. Synthesis of nano-bowls with a Janus template. *Nanoscale* **7**, 771–775 (2015).

75. Landon, P. B., Mo, A. H., Printz, A. D., Emerson, C., Zhang, C., Janetanakit, W., Colburn, D. A., Akkiraju, S., Dossou, S., Chong, B., Glinsky, G. & Lal, R. Asymmetric Colloidal Janus Particle Formation Is Core-Size-Dependent. *Langmuir* **31**, 9148–9154 (2015).

76. Witucki, G. L. A Silane Primer: Chemistry and Applications of Alkoxy Silanes. *J. Coatings Technol.* **65**, 57–60 (1993).

77. Thermo scientific. *NHS and Sulfo-NHS Instructions*. *Info* **0747**, (2011).

78. Shao, Y., Wang, L., Fu, J., Shi, C., Xu, J. & Zhu, Y. Efficient free radical generation against cancer cells by low-dose X-ray irradiation with a functional SPC delivery nanosystem. *J. Mater. Chem. B* **4**, 5863–5872 (2016).

79. Schneider, C. A., Rasband, W. S. & Eliceiri, K. W. NIH Image to ImageJ: 25 years of image analysis. *Nat. Methods* **9**, 671–675 (2012).

80. Bain, G. A. & Berry, J. F. Diamagnetic Corrections ans Pascal's Constants. *J. Chem. Educ.* **85**, 532–536 (2008).

81. Caizer, C., Savii, C. & Popovici, M. Magnetic behavior of iron oxide nanoparticles in a silica matrix. *Mater. Sci. Eng. B* **97**, 129–134 (2003).

82. Blums, E., Chukhrov, A. Y. & Rimsa, A. Some Problems of Mass Transfer in Magnetic Coilloids near a Filtrating Element in High- gradient Magnetic Separation. *J. Heat Mass Transf.* **30**, 1607–1613 (1987).

83. Blums, E., Piravii '~is, J. & Chukhrov, A. HIGH-GRADIENT MAGNETIC SEPARATION OF MAGNETIC COLLOIDS AND SUSPENSIONS. *J. Magn. Magn. Mater.* **39**, 147–151 (1983).

84. Wilkes, J. O. *Fluid Mechanics for Chemical Engineers*. (Prentice Hall, 2006).

85. Tinevez, J.-Y. & MATLAB. Simple Tracker - File Exchange - MATLAB Central.

86. Yarjanli, Z., Ghaedi, K., Esmaeili, A., Rahgozar, S. & Zarrabi, A. Iron oxide nanoparticles may damage to the neural tissue through iron accumulation, oxidative stress, and protein aggregation. *BMC Neurosci.* **18**, 1–12 (2017).

87. Faller, P., Hureau, C. & Berthoumieu, O. Role of metal ions in the self-assembly of the Alzheimer's amyloid-β peptide. *Inorg. Chem.* **52**, 12193–12206 (2013).

88. Masalov, V. M., Sukhinina, N. S., Kudrenko, E. A. & Emelchenko, G. A. Mechanism of formation and nanostructure of Stöber silica particles. *Nanotechnology* **22**, 275718 (2011).

89. Townsley, M. I. Structure and composition of pulmonary arteries, capillaries, and veins. *Compr. Physiol.* **2**, 675–709 (2012).

90. PAPAIOANNOU, THEODOROS G. STEFANADIS, C. Vasular Wall Shear Stress: Basic Principles and Methods. *Hell. J. Cardiol.* **46**, 9–15 (2005).

91. Santoyo Salazar, J., Perez, L., De Abril, O., Phuoc, L. T., Ihiawakrim, D., Vazquez, M., Greneche, J.-M., Begin-Colin, S. & Pourroy, G. Magnetic Iron Oxide Nanoparticles in 10-40 nm Range: Composition in Terms of Magnetite/Maghemite Ratio and Effect on the Magnetic Properties. *Chem. Mater* **23**, 1379–1386 (2011).

92. Goya, G. F., Berquó, T. S., Fonseca, F. C. & Morales, M. P. Static and dynamic magnetic properties of spherical magnetite nanoparticles. *Part. Size Depend. Coerc. Remanence Single-Domain Part. J. Appl. Phys.* **94**, 83908 (2003).

93. Nayek, C., Manna, K., Bhattacharjee, G., Murugavel, P. & Obaidat, I. Investigating Size- and Temperature-Dependent Coercivity and Saturation Magnetization in PEG Coated Fe3O4 Nanoparticles. *Magnetochemistry* **3**, 19 (2017).

94. Frison, R., Cernuto, G., Cervellino, A., Zaharko, O., Gian, ⊥, Colonna, M., Guagliardi, A. & Masciocchi, N. Magnetite−Maghemite Nanoparticles in the 5−15 nm Range: Correlating the Core−Shell Composition and the Surface Structure to the Magnetic Properties. A Total Scattering Study. (2013). doi:10.1021/cm403360f

95. Roca, A. G., Marco, J. F., Del, M., Morales, P. & Serna, C. J. Effect of Nature and Particle Size on Properties of Uniform Magnetite and Maghemite Nanoparticles. (2007). doi:10.1021/jp075133m

96. Vidal-Vidal, J., Rivas, J. & López-Quintela, M. A. Synthesis of monodisperse maghemite nanoparticles by the microemulsion method. *Colloids Surfaces A Physicochem. Eng.*

Asp. **288**, 44–51 (2006).

97. Nadeem, K., Krenn, H., Traussnig, T., Würschum, R., Szabó, D. V. & Letofsky-Papst, I. Effect of dipolar and exchange interactions on magnetic blocking of maghemite nanoparticles. *J. Magn. Magn. Mater.* **323**, 1998–2004 (2011).

98. Goya, G. F., Berquo, T. S. & Fonseca, F. C. Static and dynamic magnetic properties of spherical magnetite nanoparticles. *J. Appl. Phys.* **94**, 3520–3528 (2003).

99. Fu, R., Yan, Y., Roberts, C., Liu, Z. & Chen, Y. The role of dipole interactions in hyperthermia heating colloidal clusters of densely-packed superparamagnetic nanoparticles. *Sci. Rep.* **8**, 4704 (2018).

100. Zhou, Z., Tian, R., Wang, Z., Yang, Z., Liu, Y., Liu, G., Wang, R., Gao, J., Song, J., Nie, L. & Chen, X. Artificial local magnetic field inhomogeneity enhances T2 relaxivity. *Nat. Commun.* **8**, 15468 (2017).

101. Xu, H., Medina-Sánchez, M., Magdanz, V., Schwarz, L., Hebenstreit, F. & Schmidt, O. G. Sperm-Hybrid Micromotor for Targeted Drug Delivery. *ACS Nano* **12**, 327–337 (2018).

102. Charoenphol, P., Onyskiw, P. J., Carrasco-Teja, M. & Eniola-Adefeso, O. Particle-cell dynamics in human blood flow: Implications for vascular-targeted drug delivery. *J. Biomech.* **45**, 2822–2828 (2012).

103. Müller, K., Fedosov, D. A. & Gompper, G. Margination of micro- and nano-particles in blood flow and its effect on drug delivery. *Sci. Rep.* **4**, 4871 (2015).

104. Craparo, E., D'Apolito, R., Giammona, G., Cavallaro, G. & Tomaiuolo, G. Margination of Fluorescent Polylactic Acid–Polyaspartamide based Nanoparticles in Microcapillaries In Vitro: the Effect of Hematocrit and Pressure. *Molecules* **22**, 1845 (2017).

105. Nadkarni, R., Barkley, S. & Fradin, C. A comparison of methods to measure the magnetic moment of magnetotactic bacteria through analysis of their trajectories in external magnetic fields. *PLoS One* **8**, e82064 (2013).

106. Zahn, C., Keller, S., Toro-Nahuelpan, M., Dorscht, P., Gross, W., Laumann, M., Gekle, S., Zimmermann, W., Schüler, D. & Kress, H. Measurement of the magnetic moment of single Magnetospirillum gryphiswaldense cells by magnetic tweezers. *Sci. Rep.* **7**, 3558 (2017).

107. GE Healthcare. *MR Safety Guide Operator Manual GE Medical Systems, LLC, doing business as GE Healthcare MR Safety Guide*. (2013).

108. Usov, N. A. & Ya Liubimov, B. *Magnetic nanoparticle traveling in external magnetic field*.

109. Wagner, T., Lipinski, H.-G. & Wiemann, M. Dark field nanoparticle tracking analysis for size characterization of plasmonic and non-plasmonic particles. *J. Nanopart. Res.* **16**, 2419 (2014).

110. Ueno, H., Nishikawa, S., Iino, R., Tabata, K. V., Sakakihara, S., Yanagida, T. & Noji, H. Simple Dark-Field Microscopy with Nanometer Spatial Precision and Microsecond Temporal Resolution. *Biophys. J.* **98**, 2014–2023 (2010).

111. Huntsman, L. L., Gams, E., Johnson, C. C. & Fairbanks, E. Transcutaneous determination of aortic blood-flow velocities in man. *Am. Heart J.* **89**, 605–612 (1975).

112. GABE, I. T., GAULT, J. H., ROSS, J., MASON, D. T., MILLS, C. ., SCHILLINGFORD, J.

P. & BRAUNWALD, E. Measurement of Instantaneous Blood Flow Velocity and Pressure in Conscious Man with a Catheter-Tip Velocity Probe. *Circ.* **40**, 603–614 (2018).

113. Demertzis, S., Hurni, S., Stalder, M., Gahl, B., Herrmann, G. & Van den Berg, J. Aortic arch morphometry in living humans. *J. Anat.* **217**, 588–96 (2010).